Oxidation-driven mtDNA B-Z transition activates ZBP1 to mediate acetaminophen hepatotoxicity

Zhang-Hua Yang[*1#], Bo-Xin Zhang[1#], Huan-Feng Ye[2#], Liang Shi[1#], Rui Gong[1#], Zhi-Yu Cai[1], Qiang Chen[1], Lei Wu[1], Jia Huang[1], Le Zhang[3], Huipeng Jiao[4], Pinglong Xu[4], Qinjie Weng[5], Jie Zhang[6], Jinheng Pan[7], Shan Feng[7], Haibing Zhang[8], Xian Shen[9], Mingyu Chen[*1], Wei Mo[*1,2]

Acetaminophen (APAP) overdose induces mitochondrial damage in hepatocytes, leading to secondary toxicity that resists N-acetylcysteine (NAC) treatment and culminates in hepatocyte death and acute liver failure (ALF)[1]. The underlying mechanisms remain poorly understood, often necessitating liver transplantation[2]. Here, we identify oxidative modification-driven B-to-Z transitions in mitochondrial DNA (mtDNA) as the central pathological driver of APAP-induced ALF. Upon APAP exposure, oxidized mtDNA fragments leak into the cytosol, activating ZBP1 signaling via its Zα domain. This recognition triggers ZBP1-dependent apoptotic signaling, and genetic inhibition of either *Zbp1*, *Mavs* or *Casp8* mitigates liver damage and improves survival. Using synthetic dGdC duplexes, we demonstrate that 8-oxoG substitution, even under physiological salt concentrations, is sufficient to induce Z-DNA formation, enabling specific ZBP1 binding through its Zα domain. The 8-oxoG repair enzyme OGG1[3], activated by TH10785[4], removes 8-oxoG modifications and reverses the Z-DNA conformation back to B-DNA. In mice with lethal APAP toxicity, delayed NAC treatment results in 50% mortality. In contrast, TH10785 monotherapy increases survival rate to 90%, while its combination with NAC achieves 100% survival. These results define the oxidized mtZ-DNA-ZBP1 axis as a critical driver of APAP hepatotoxicity, providing fundamental insights into DNA conformational dynamics and therapeutic opportunities in drug-induced liver failure.

https://doi.org/10.15302/vita.2026.04.0029

INTRODUCTION

The liver serves as one of the principal detoxification organs in the human body, playing a critical role in the metabolism and elimination of toxins, drugs, and other deleterious substances. Nevertheless, the metabolic processing of drugs can also induce hepatic injury, a condition referred to as Drug-Induced Liver Injury (DILI)[5,6]. Acetaminophen (APAP), a widely utilized component in cold medications, can provoke extensive hepatocyte necrosis when consumed in excessive amounts. The central mechanism underlying its hepatotoxicity is mitochondrial dysfunction[7]. APAP is primarily metabolized by the cytochrome P450 enzyme CYP2E1, yielding the highly reactive and toxic metabolite N-acetyl-p-benzoquinone imine (NAPQI)[8]. NAPQI covalently binds to mitochondrial inner membrane proteins, disrupting the electron transport chain (ETC), altering mitochondrial membrane permeability, and triggering the overproduction of reactive oxygen species (ROS)[9,10]. These events culminate in mitochondrial impairment and subsequent hepatocyte necrosis. During the initial phase of APAP intoxication, the abundant availability of glutathione (GSH) facilitates the detoxification of NAPQI, thereby attenuating its direct deleterious effects on mitochondria[11]. However, beyond 8-h post-APAP overdose, mitochondrial damage and ROS-driven oxidative stress initiate a cascade of extensive secondary injury to hepatocytes. This secondary damage cannot be mitigated by GSH administration beyond this critical 8-h window, leading to irreversible and widespread hepatocyte death and the onset of acute liver failure (ALF)[1]. Therefore, elucidating the core pathological mechanisms underlying the secondary damage induced by APAP overdose is pivotal for developing strategies to reduce the incidence of APAP-induced ALF.

RESULTS

Cytoplasmic mtDNA activates ZBP1 to drive hepatocyte death

Mitochondrial damage-induced leakage of mitochondrial DNA (mtDNA) into the cytoplasm is a key trigger of immune responses and cell death, contributing to the pathogenesis of various diseases[12]. Similarly, APAP-induced mitochondrial injury leads to the cytosolic release of mtDNA. In both APAP-treated murine livers (Supplementary Fig. S1a–c) and the hepatocyte cell line AML12 (Supplementary Fig. S1b, d), a substantial accumulation of cytosolic double-stranded DNA

1. Department of General Surgery of Sir Run Run Shaw Hospital; Department of Immunology of School of Basic Medical Sciences, Zhejiang University School of Medicine, Liangzhu Laboratory, Zhejiang University, Hangzhou, Zhejiang, China. 2. State Key Laboratory of Cellular Stress Biology, School of Life Sciences, Xiamen University, Xiamen, Fujian, China. 3. The "5+3" integrated program of clinical medicine, Zhejiang University School of Medicine, Zhejiang University, Hangzhou, Zhejiang, China. 4. Zhejiang Key Laboratory of Molecular Cancer Biology, Life Sciences Institute, Zhejiang University, Hangzhou, Zhejiang, China. 5. Center for Drug Safety Evaluation and Research, Zhejiang Province Key Laboratory of Anti-Cancer Drug Research, College of Pharmaceutical Sciences, Zhejiang University, Hangzhou, Zhejiang, China. 6. Innovation Centre for Information, Binjiang Institute of Zhejiang University, Hangzhou, Zhejiang, China. 7. Key Laboratory of Structural Biology of Zhejiang Province, Mass Spectrometry & Metabolomics Core Facility, The Biomedical Research Core Facility, Westlake University, Hangzhou, Zhejiang, China. 8. Shanghai Institute of Nutrition and Health, University of Chinese Academy of Sciences, Chinese Academy of Sciences, Shanghai, China. 9. Department of Gastrointestinal Surgery, The First Affiliated Hospital of Wenzhou Medical University, Wenzhou, Zhejiang, China. #These authors contributed equally to this work. *Correspondence: Zhang-Hua Yang (zhanghuayang@zju.edu.cn), Mingyu Chen (mychen@zju.edu.cn), Wei Mo (weimo@zju.edu.cn)
Received: February 12, 2026; Accepted: April 28, 2026; Published: May 11, 2026

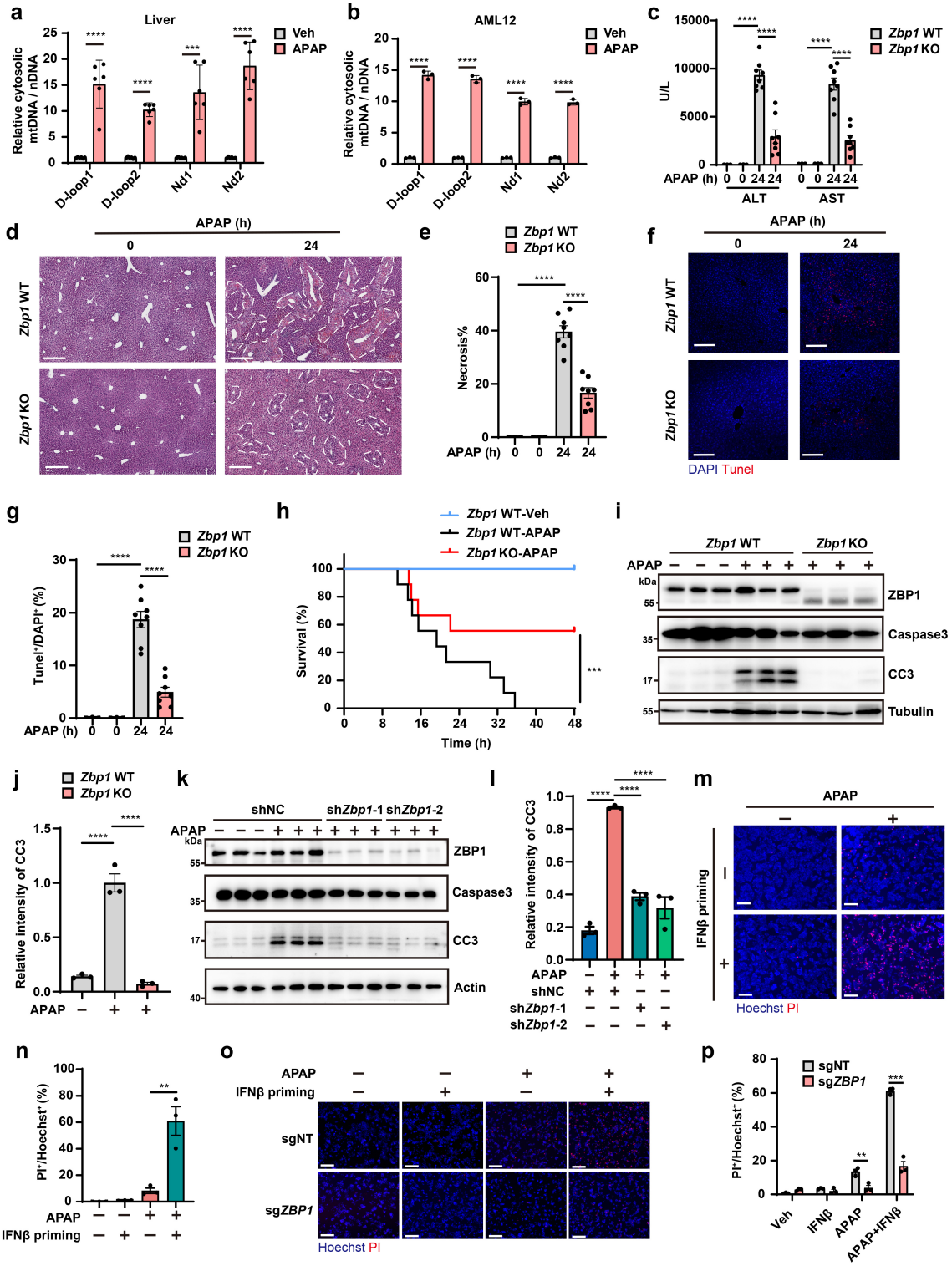

Fig. 1 Cytoplasmic mtDNA activates ZBP1, not cGAS, to drive hepatocyte death. a, **b** Relative amount of cytosolic mtDNA release in cytosol fraction of liver from WT mice (**a**) or AML12 cells (**b**) treated with or without APAP for 24 h. **a** 300 mg/kg intraperitoneally (i.p.) for mice, *n* = 6 mice. **b** 10 mM for cell, *n* = 3 independent samples. **c** Serum ALT and AST levels were determined in *Zbp1* WT and *Zbp1* KO mice. 0 h: *n* = 3 mice per genotype, 24 h: *n* = 8 mice per genotype. **d** H&E staining of the liver sections from *Zbp1* WT and *Zbp1* KO mice. Scale bars, 300 μm. **e** Necrotic areas were encircled and quantified. 0 h: *n* = 3 mice, 24 h: *n* = 8 mice. **f**, **g** Representative images (**f**) and quantitative analysis (**g**) of TUNEL staining in liver tissues from *Zbp1* WT and *Zbp1* KO mice. 0 h: *n* = 3 mice, 24 h: *n* = 8 mice. Scale bars, 100 μm. **h** Survival curves of *Zbp1* WT and *Zbp1* KO mice treated with a lethal dose of APAP (550 mg/kg, i.p.), *n* = 9 mice per genotype. **i**, **j** Western blotting (**i**) and quantitative analysis (**j**) of liver proteins from *Zbp1* WT and *Zbp1* KO mice treated with or without APAP for 24 h. *n* = 3 mice per group. CC3: cleaved caspase-3. **k**, **l** Western blotting (**k**) and quantitative analysis (**l**) of shNC (non-target control) or sh*Zbp1* AML12 cells treated with or without APAP for 24 h. *n* = 3 independent samples. **m**, **n** Representative images (**m**) and quantitative analysis (**n**) of Hoechst and PI staining in HepG2 cells pretreated with or without IFNβ for 30 h, followed by treatment with vehicle or APAP (20 mM) for 24 h. *n* = 3 independent samples. Scale bars, 200 μm. **o**, **p** Representative images (**o**) and quantitative analysis (**p**) of Hoechst and PI staining in sgNT (non-target control) and sg*ZBP1* HepG2 cells pretreated with or without IFNβ for 30 h, followed by vehicle or APAP (20 mM) treatment for 24 h. *n* = 3 independent samples. Scale bars, 200 μm. Data are mean ± SEM. Statistical analyses were performed using unpaired two-tailed Student's *t*-test (**a**, **b**, **n**, **p**), one-way analysis of variance (ANOVA) post hoc Dunnett's tests (**c**, **e**, **g**, **j**, **l**), and Mantel–Cox tests (**h**); ns, not significant; $^{*}P < 0.05$; $^{**}P < 0.01$; $^{***}P < 0.001$; $^{****}P < 0.0001$. For gel source data, see Supplementary Data S1.

(dsDNA) signal was detected (Fig. 1a, b; Supplementary Fig. S1e, f), which was confirmed to be mtDNA-derived (Fig. 1a, b). This release occurred without a significant increase in overall mitochondrial mass (Supplementary Fig. S1g, h), indicating that the cytosolic mtDNA accumulation results from specific release rather than a generalized increase in mitochondrial mass.

Conventionally, aberrantly leaked cytosolic mtDNA is recognized by cyclic GMP-AMP synthase (cGAS), triggering innate immune signaling[13]. However, in APAP-treated cells, cytosolic mtDNA failed to activate cGAS, as indicated by the absence of increased cGAMP production (Supplementary Fig. S1i, j) — the enzymatic product of cGAS activation, and the lack of phosphorylation of its downstream effector, TANK-binding kinase 1 (TBK1) (Supplementary Fig. S1k). Consistent with these findings, genetic ablation of *cGAS* did not confer protection against APAP-induced liver injury in mice. Compared to wild-type (WT) controls, cGAS-deficient mice showed no improvement of liver function as indicated by serum markers such as alanine aminotransferase (ALT) and aspartate aminotransferase (AST) (Supplementary Fig. S1l), nor a reduction in TUNEL-positive hepatocytes or necrotic areas (Supplementary Fig. S1m–p). These findings may be attributed to the extremely low expression levels of key components of DNA-sensing pathways in hepatocytes[14,15], particularly the cGAS, as previously reported and also observed in our study.

Other cytosolic DNA sensors, including interferon gamma-inducible protein 16 (IFI16), DEAD-box helicase 41 (DDX41), and absent in melanoma 2 (AIM2), are known to activate inflammatory cytokine responses[16-18]. However, 24-h post APAP treatment, no significant changes were observed in the levels of interferons or pro-inflammatory cytokines such as tumor necrosis factor (TNF), interleukin-1β (IL-1β), and interleukin-6 (IL-6) (Supplementary Fig. S1q). These findings suggest that APAP-induced cytosolic mtDNA does not trigger conventional innate immune signaling pathways.

Intriguingly, Z-DNA binding protein 1 (ZBP1), a non-canonical cytosolic dsDNA sensor that is constitutively expressed in the liver (Supplementary Fig. S1r), does not primarily induce type I interferon responses but is instead implicated in the direct initiation of cell death[19,20]. Based on these observations, we hypothesized that cytosolic mtDNA released upon APAP treatment is sensed by ZBP1, which subsequently drives hepatocyte death.

In the APAP-induced liver injury model, genetic ablation of *Zbp1* confers significant protection against hepatic dysfunction in mice as indicated by decreased levels of ALT and AST (Fig. 1c). Histopathological analysis using hematoxylin and eosin (H&E) staining demonstrated a substantial reduction in necrotic areas in the livers of *Zbp1* knockout (KO) mice compared to those of WT controls (Fig. 1d, e). Quantification of TUNEL staining further revealed that the proportion of TUNEL-positive cells in *Zbp1* KO livers decreased to 5%, indicating a marked reduction in cell death (Fig. 1f, g). Additionally, following APAP administration, the infiltration of immune cells, particularly neutrophils, was significantly attenuated in the livers of *Zbp1* KO mice relative to WT mice (Supplementary Fig. S1s, t). In a survival study, treatment with a lethal dose of APAP resulted in a 100% mortality rate within 48 h in WT mice; however, *Zbp1* KO reduced the mortality rate to 40% (Fig. 1h), highlighting the protective role of ZBP1 deficiency in mitigating APAP-induced lethality.

ZBP1 mediates hepatocyte apoptosis

Building on these findings, we further elucidated the mechanism through which ZBP1 drives hepatocyte cell death. Although ZBP1 is known to recruit RIPK3 via its RHIM domain to initiate necroptosis[21], this pathway is not operational in hepatocytes due to the absence of RIPK3 expression, and accordingly, necroptosis (pMLKL) was not observed in hepatocytes following APAP treatment (Supplementary Fig. S2a). Consistent with this, genetic ablation of *Ripk3* or *Mlkl* failed to confer protection against APAP-induced liver injury (Supplementary Fig. S2b), ruling out necroptosis as a contributing mechanism. Beyond necroptosis, ZBP1 has been implicated in the regulation of apoptosis. In APAP-treated livers, robust caspase-3 cleavage was detected, whereas *Zbp1* KO livers exhibited no such activation of caspase-3 (Fig. 1i, j), suggesting a critical role for ZBP1 in APAP-induced apoptotic cell death. To address the potential confounding effects of non-hepatocyte contributions in liver tissue extracts, we validated these findings in a murine hepatocyte cell line, where APAP treatment similarly induced caspase-3 cleavage and apoptosis, and *Zbp1* knockdown effectively suppressed caspase-3 activation and apoptosis (Fig. 1k, l; Supplementary Fig. S2c). To extend these findings to a human model, we validated this mechanism in HepG2 cells, a human hepatocyte cell line that expresses significant levels of the key APAP-metabolizing enzyme CYP2E1 (Supplementary Fig. S2d). Since this cell line does not constitutively express ZBP1, we utilized IFN priming to induce its expression (Supplementary Fig. S2e). In IFN-primed HepG2 cells, APAP induced robust apoptotic cell death, evidenced by caspase-3 activation and propidium iodide (PI) staining (Fig. 1m, n; Supplementary Fig. S2e, f). Critically, sgRNA-mediated knockout of *Zbp1* in HepG2 nearly completely blocked APAP-induced cell death (Fig. 1o, p; Supplementary Fig. S2g).

ZBP1-mediated apoptosis is primarily executed via RIPK1–FADD–caspase-8 complex[22]. Accordingly, in APAP-treated liver samples, activation of caspase-8 but not caspase-9 was observed (Supplementary Fig. S3a, b). The obvious activation of both caspase-8 and downstream caspase-3 within 8 h post APAP suggests a direct role for caspase-8-mediated apoptosis in the initial cell death cascade (Supplementary Fig. S3c, d). Genetic ablation of *Zbp1* abrogated APAP-induced caspase-8 and caspase-3 activation in both liver and hepatocyte cell line AML12 (Fig. 1i, j; Supplementary Figs. S3e, f), confirming the dependence of ZBP1 for this apoptotic pathway. Furthermore, *Ripk3*$^{-/-}$*Casp8*$^{-/-}$ double-KO mice were highly resistant to APAP-induced liver injury, hepatocyte apoptosis and mouse lethality (Fig. 2a–h). As hepatocytes lack RIPK3 and that *Ripk3* knockout alone is not protective (Supplementary Fig. S2b), these results point to caspase-8 as the key mediator of ZBP1-dependent apoptosis in hepatocytes. This conclusion was further substantiated by the marked protection observed in mice with AAV-mediated, hepatocyte-specific *Casp8* knockout (Fig. 2i–o).

However, genetic deletion of *Ripk1* or *Fadd* did not mitigate APAP-induced apoptotic signaling in hepatocyte cell line AML12 (Supplementary Fig. S4a, b), suggesting that ZBP1-triggered apoptosis occurs independently of the canonical RIPK1–FADD complex. Supporting this notion, *Ripk1*,*Fadd*,*Ripk3* triple-knockout (TKO) mice were not protected from APAP-induced liver injury (Supplementary Fig. S4c). This finding aligns with a prior report that hepatocyte-restricted *Ripk1* knockout did not protect mice from APAP-induced liver toxic-

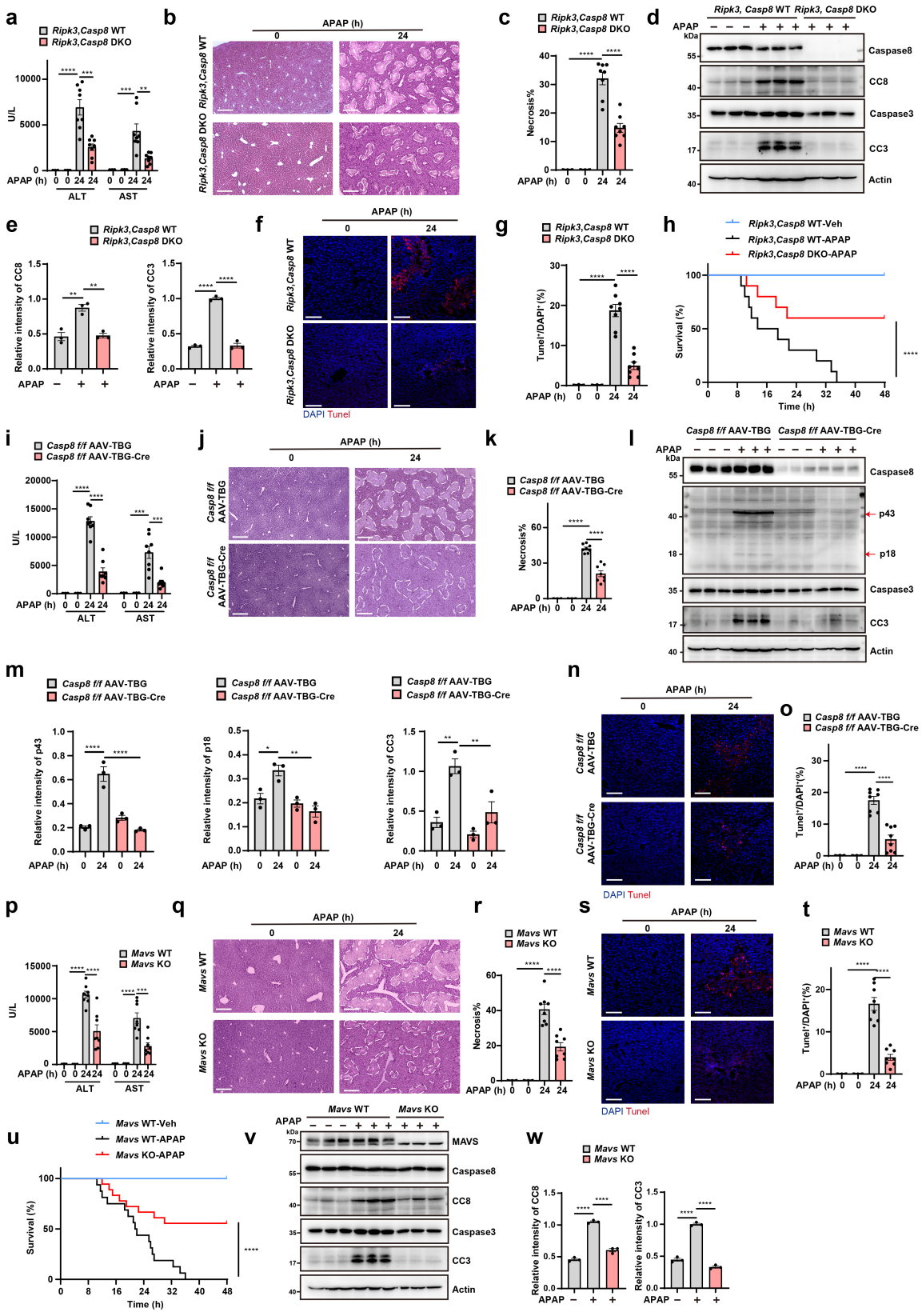

Fig. 2 ZBP1 activates caspase-8-dependent apoptosis via MAVS. a Serum ALT and AST levels were determined in *Ripk3*,*Casp8* WT and *Ripk3*,*Casp8* double knockout (DKO) mice. 0 h: *n* = 3 mice per genotype, 24 h: *n* = 8 mice per genotype. **b** H&E staining of the liver sections from *Ripk3*,*Casp8* WT and *Ripk3*,*Casp8* DKO mice. **c** Necrotic areas were encircled and quantified. 0 h: *n* = 3 mice, 24 h: *n* = 8 mice. Scale bars, 300 μm. **d**, **e** Western blotting (**d**) and quantitative analyses (**e**) of liver proteins from *Ripk3*,*Casp8* WT and *Ripk3*,*Casp8* DKO mice treated with or without APAP for 24 h. *n* = 3 mice per group. CC3: cleaved caspase-3, CC8: cleaved caspase-8. **f**, **g** Representative images (**f**) and quantitative analysis (**g**) of TUNEL staining in liver tissues from *Ripk3*,*Casp8* WT and *Ripk3*,*Casp8* KO mice. 0 h: *n* = 3 mice, 24 h: *n* = 8 mice. Scale bars, 100 μm. **h** Survival curves of *Ripk3*,*Casp8* WT and *Ripk3*,*Casp8* KO mice treated with a lethal dose of APAP (550 mg/kg, i.p.), *n* = 10 mice per genotype. **i** Serum ALT and AST levels were determined in *Casp8*$^{f/f}$ mice injected with AAV-TBG-control or AAV-TBG-Cre. 0 h: *n* = 3 mice per genotype, 24 h: *n* = 8 mice per genotype. **j** H&E staining of the liver sections from *Casp8*$^{f/f}$ mice injected with AAV-TBG-control or AAV-TBG-Cre. **k** Necrotic areas were encircled and quantified. 0 h: *n* = 3 mice, 24 h: *n* = 8 mice. Scale bars, 300 μm. **l**, **m** Western blotting (**l**) and quantitative analysis (**m**) of liver proteins from *Casp8*$^{f/f}$ mice injected with AAV-TBG-control or AAV-TBG-Cre, followed by treatment with or without APAP for 24 h. *n* = 3 mice per group. CC3: cleaved caspase-3, CC8: cleaved caspase-8. **n**, **o** Representative images (**n**) and quantitative analysis

(**o**) of TUNEL staining in liver tissues from *Casp8*$^{f/f}$ mice injected with AAV-TBG-control or AAV-TBG-Cre. 0 h: *n* = 3 mice, 24 h: *n* = 8 mice. Scale bars, 100 μm. **p** Serum ALT and AST levels were determined in *Mavs* WT and *Mavs* KO mice. 0 h: *n* = 3 mice per genotype, 24 h: *n* = 8 mice per genotype. **q** H&E staining of the liver sections from *Mavs* WT and *Mavs* KO mice. **r** Necrotic areas were encircled and quantified. 0 h: *n* = 3 mice, 24 h: *n* = 8 mice. Scale bars, 300 μm. **s**, **t** Representative images (**s**) and quantification analyses (**t**) of TUNEL staining in liver tissues from *Mavs* WT and *Mavs* KO mice. 0 h: *n* = 3 mice, 24 h: *n* = 8 mice. Scale bars, 100 μm. **u** Survival curves of *Mavs* WT and *Mavs* KO mice treated with a lethal dose of APAP (550 mg/kg, i.p.), *n* = 16 *Mavs* WT mice, *n* = 18 *Mavs* KO mice. **v**, **w** Western blotting (**v**) and quantitative analyses (**w**) of liver proteins from *Mavs* WT and *Mavs* KO mice treated with or without APAP for 24 h. *n* = 3 mice per group. CC3: cleaved caspase-3, CC8: cleaved caspase-8. Data are mean ± SEM. Statistical analyses were performed using one-way ANOVA post hoc Dunnett's tests (**a**, **c**, **e**, **g**, **i**, **k**, **m**, **o**, **p**, **r**, **t** and **w**) and Mantel–Cox tests (**h** and **u**); ns, not significant; $^{*}P < 0.05$; $^{**}P < 0.01$; $^{***}P < 0.001$; $^{****}P < 0.0001$. For gel source data, see Supplementary Data S1.

ity [23]. We thus considered an alternative mechanism.

Given that the mitochondrial adaptor MAVS can activate caspase-8 to induce apoptosis[24,25] and has been shown to functionally interact with ZBP1[26], we hypothesized a role for MAVS in this context. We first confirmed that MAVS can induce the activation of both caspase-8 and its downstream effector caspase-3, thereby validating its pro-apoptotic function (Supplementary Fig. S4d–f). Furthermore, consistent with prior reports[24], we found that MAVS-induced caspase-3 activation is dependent on caspase-8 (Supplementary Fig. S4e). We also confirmed the physical interaction between ZBP1 and MAVS by co-immunoprecipitation (co-IP; Supplementary Fig. S4g). Additional co-IP experiments revealed that ZBP1 with mutated RHIM domains (RHIM1 and RHIM2) exhibited attenuated binding to MAVS compared with WT-ZBP1 (Supplementary Fig. S4h). Functionally, knockout of *Mavs* in AML12 cells significantly decreased APAP-induced activation of caspase-8 and caspase-3, similar to *Zbp1* knockout, supporting that MAVS is required for APAP-induced apoptosis (Supplementary Fig. S4i–k). More importantly, *Mavs* KO mice were significantly protected from APAP-induced liver injury, hepatocyte cell death and mouse lethality (Fig. 2p–u), comparable to *Zbp1* KO mice. Critically, this protection was associated with a complete abolition of both caspase-8 and caspase-3 activation, without affecting ZBP1 expression (Fig. 2v, w; Supplementary Fig. S4l). To determine whether MAVS and ZBP1 operate in the same pathway, we performed a genetic epistasis analysis. In AML12 cells, knockout of *Mavs* in a *Zbp1*-deficient background did not produce an additive reduction in APAP-induced caspase-3 cleavage compared to *Zbp1* knockout alone (Supplementary Fig. S4m, n). This indicates that ZBP1 and MAVS function within the same signaling pathway in the APAP hepatotoxicity. Furthermore, using proximity ligation assay (PLA), we detected a significant interaction between ZBP1 and MAVS in APAP-treated AML12 cells, reinforcing the conclusion that ZBP1 engages MAVS to activate caspase-8 and downstream apoptosis (Supplementary Figs. S4o, p). We noted that the ZBP1-MAVS pathway appears to be specifically engaged during APAP-induced injury, as knockdown of MAVS had no effect on established ZBP1-dependent cell death induced by splicing inhibition[27,28] (Supplementary Fig. S4q, r). Collectively, these data support a model wherein ZBP1 activates caspase-8-dependent apoptosis via MAVS, independently of RIPK1-FADD axis.

We also explored the possibility of pyroptosis in this context. However, no evidence of Gasdermin D-mediated pyroptosis was detected in APAP-treated livers (Supplementary Fig. S4s), further corroborating the lack of AIM2 activation despite the presence of cytosolic mtDNA. Additionally, Gasdermin E (GSDME), whose cleavage is caspase-3-dependent, remained intact following APAP treatment (Supplementary Fig. S4s), reinforcing the notion that APAP-induced caspase-3 activation specifically drives apoptosis rather than Gasdermin E-mediated pyroptosis. Collectively, these findings indicate that the critical pathological mechanism underlying APAP-induced liver injury involves the release of mtDNA into the cytoplasm, which subsequently activates the ZBP1-mediated apoptotic pathway, leading to hepatocyte death.

ZBP1 binds to Z-DNA derived from released mitochondrial DNA

ZBP1 functions as a critical sensor of left-handed Z-form nucleic acids (Z-DNA/Z-RNA)[29-33], raising the possibility that APAP-induced hepatocyte injury triggers the formation of Z-nucleic acids (ZNA). To investigate this hypothesis, we employed the Z22 antibody, which selectively recognizes ZNA, including both Z-DNA and Z-RNA, to detect their presence in APAP-treated hepatocytes. As shown in Fig. 3a–c, significant accumulation of ZNA was observed in both liver tissues, *ex vivo* hepatocyte and cultured hepatocyte AML12 cells following APAP exposure. Notably, the ZNA signal detected in the livers of APAP-treated mice, primary hepatocyte and APAP-stimulated AML12 cells was abolished by DNase I treatment but remained unaffected by RNase A (Fig. 3a–f), confirming that the observed ZNA signal was primarily derived from DNA. The APAP-induced Z-DNA accumulation was comparable between WT and *Zbp1* KO mice (Supplementary Fig. S5a, b), indicating that Z-DNA formation occurs independently of ZBP1.

A substantial fraction of Z-DNA colocalized with the mitochondrial marker TOM20, while a portion was detected outside mitochondria (Fig. 3b, c), suggesting that the Z-DNA may originate from leaked mtDNA. The majority of ZNA signals in the cytosol did not co-localize with mitochondrial-derived vesicles (MDVs) (Supplementary Fig. S5c, d), suggesting that the mtDNA is largely released freely into the cytosol rather than remaining vesicle-encapsulated. To directly determine the source of Z-DNA that engages ZBP1 upon APAP stimulation, we performed ZBP1 immunoprecipitation (IP) followed by qPCR analysis to distinguish nuclear vs mtDNA (Fig. 3g). The results demonstrated that, following APAP exposure, ZBP1 was specifically bound to mtDNA, as indicated by the enrichment of mitochondrial markers Nd1 and Nd2, while markers of nuclear DNA, including LINE1 and RNA18S, were absent (Fig. 3g). Consistent with this, depletion of mtDNA using ethidium bromide (EtBr) (Supplementary Fig. S5e) abolished APAP-induced Z-DNA formation (Fig. 3h, i). Furthermore, EtBr-mediated mtDNA depletion significantly attenuated APAP-induced apoptotic signaling (Fig. 3j, k), reinforcing the critical role of mtDNA-derived Z-DNA in promoting cell death pathways. Furthermore, nearly all APAP-induced dead cells (TUNEL-positive cells) were also positive for Z-DNA (Supplementary Fig. S5f, g). This strong correlation reinforces that Z-DNA formation is a driving force of the cell death pathway in this model.

The N-terminal Zα domain of ZBP1 is essential for its interaction with dsDNA, and point mutations in the Zα1 and Zα2 subdomains effectively disrupted this binding. Consistent

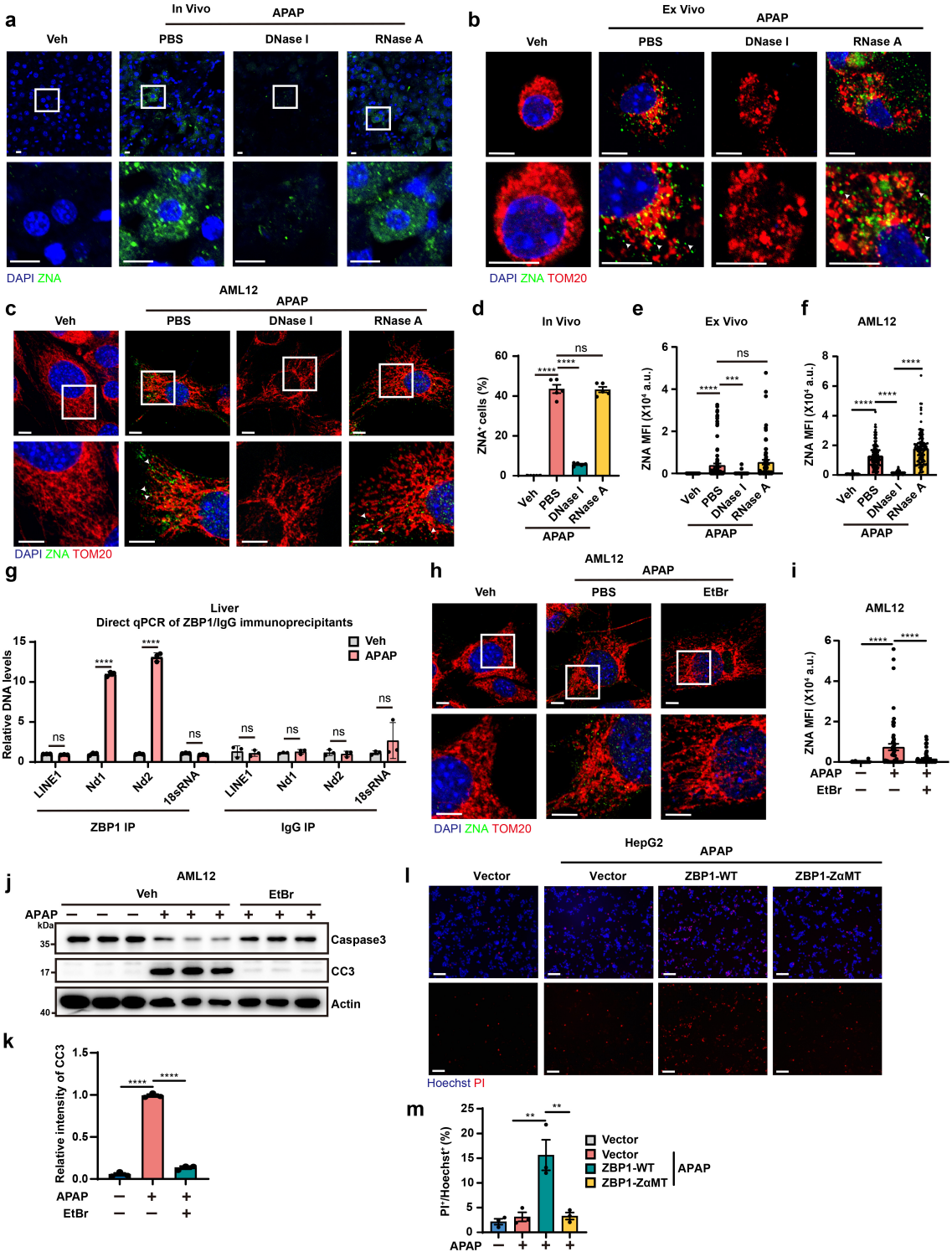

Fig. 3 ZBP1 binds to Z-DNA derived from released mtDNA. a Immunofluorescence staining of ZNA (green) with anti-ZNA antibody with or without DNase I (25 U/mL) or RNase A (1 mg/mL) treatment in the liver of WT mice treated with Vehicle or APAP (300 mg/kg) for 24 h. Scale bars, 10 μm. **b** Immunofluorescence staining of ZNA (green) and TOM20 (red) in the hepatocytes isolated from WT mice treated with Vehicle or APAP (300 mg/kg) for 24 h. Scale bars, 10 μm. **c** Immunofluorescence staining of ZNA (green) and TOM20 (red) in the AML12 cells treated with Vehicle or APAP (10 mM) for 24 h. Scale bars, 10 μm. **b**, **c** The white arrow indicates the released mtDNA. **d** Quantification of the percentage of ZNA positive cells in **a**. *n* = 5 mice per group and more than 100 cells were used for quantification. **e** Mean fluorescence intensity (MFI) (arbitrary units, a.u.) of the ZNA signal in **b**. n > 70 cells per group. **f** MFI (arbitrary units, a.u.) of the ZNA signal in **c**. n > 110 cells per group. **g** qPCR analysis of ZBP1-binding DNAs enriched by anti-ZBP1 or anti-IgG immunoprecipitation in liver of WT mice treated with Vehicle or APAP (300 mg/kg) for 24 h. *n* = 3 mice per group. **h** Immunofluorescence staining of ZNA (green) in the AML12 cells with or without mtDNA depletion by EtBr (400 ng/mL) treatment for 6 days and stimulated with Vehicle or APAP (10 mM) for 24 h. Scale bars, 10 μm. **i** Quantification of the percentage of ZNA positive cells in **h**. *n* > 50 cells per group. **j**, **k** Western blotting (**j**) and quantitative analyses (**k**) of the AML12 cells with or without mtDNA depletion by EtBr (400 ng/mL) treatment for 6 days and stimulated with Vehicle or APAP (10 mM) for 24 h. *n* = 3 independent samples. **l**, **m** Representative images (**l**) and quantitative analysis (**m**) of Hoechst and PI staining in HepG2 cells expressing either human ZBP1-WT or human ZBP1-Zα mutant (ZαMT), followed by treatment with vehicle or APAP (20 mM) for 12 h. *n* = 3 independent samples. Scale bars, 200 μm. Data are mean ± SEM. Statistical analysis was performed using one-way ANOVA post hoc Dunnett's tests (**d**, **e**, **f**, **i**, **k** and **m**) and two-way ANOVA post hoc Bonferroni's tests (**g**); ns, not significant; $^{*}P < 0.05$; $^{**}P < 0.01$; $^{***}P < 0.001$; $^{****}P < 0.0001$. For gel source data, see Supplementary Data S1.

with the mitochondrial origin of the Z-DNA, this mutation completely abrogated the enrichment of mtDNA in the ZBP1 immunoprecipitation (Fig. 3g; Supplementary Fig. S6a), confirming that mtDNA specifically binds to the Zα domains of ZBP1. To definitively confirm the functional requirement of the Zα domains, we reconstituted *Zbp1*-KO AML12 cells with either WT ZBP1 or a Zα mutant. Expression of WT ZBP1 fully restored cellular sensitivity to APAP-induced apoptosis, whereas the Zα mutant did not (Supplementary Fig. S6b). We further validated this finding in a human context by expressing ZBP1 in human HepG2 hepatocytes, where we observed a similar requirement for the Zα domains to confer APAP sensitivity (Fig. 3l, m; Supplementary Fig. S6c). These results conclusively demonstrate that the ZNA sensing function of ZBP1 is essential for initiating the cell death pathway.

In the APAP-induced liver injury model, mice expressing ZBP1 Zα mutants exhibited hepatoprotection comparable to that observed in *Zbp1* KO mice (Supplementary Fig. S6d). This protection was characterized by reduced apoptosis (Supplementary Fig. S6e–h), diminished necrotic regions (Supplementary Fig. S6i, j), and decreased immune cell infiltration (Supplementary Fig. S6k, l). These findings indicate that ZBP1-mediated recognition of Z-DNA plays a pivotal role in APAP-induced hepatocyte death and liver injury, underscoring the pathogenic significance of mtDNA-derived Z-DNA in APAP toxicity.

Oxidative stress induces mtDNA fragmentation and cytoplasmic leakage in APAP-induced liver injury

In the context of APAP-induced oxidative stress, excessive ROS mediate mtDNA oxidation, leading to its fragmentation (Fig. 4a; Supplementary Figs. S1b, 7a). 8-Oxoguanine (8-hydroxyguanine, 8-oxoG) is one of the most common DNA lesions resulting from ROS. Using an 8-oxoG-specific antibody, we observed a significant elevation in cytoplasmic oxidized DNA levels in the APAP-induced liver injury model (Fig. 4b; Supplementary Fig. S1b, c). Additionally, APAP-treated hepatocytes exhibited an approximately 16-fold increase in cytoplasmic oxidized DNA (Fig. 4c; Supplementary Fig. S1b, d). The excess accumulation of 8-oxoG in mtDNA following APAP treatment was further validated by mass spectrometry (Supplementary Figs. S1b, 7b, c). Notably, treatment with the mitochondrial-targeted ROS scavenger MitoQ markedly reduced cytoplasmic oxidized DNA levels (Fig. 4d–f; Supplementary Fig. S7d). This reduction was accompanied by a substantial decrease in both intra-mitochondrial and cytoplasmic Z-DNA (Fig. 4g, h), suggesting that mtDNA oxidation promotes Z-DNA formation. Consistently, ROS depletion by MitoQ also significantly attenuated APAP-induced apoptotic signaling (Fig. 4i, j).

Next, we sought to elucidate the mechanism underlying oxidized mtDNA release. Previous studies have proposed that oxidized mtDNA undergoes cleavage by Flap Endonuclease 1 (FEN1) to generate short oxidized mtDNA fragments before their release into the cytoplasm[34]. However, in APAP-treated hepatocytes, downregulation of FEN1 did not affect either the cytoplasmic leakage of oxidized mtDNA (Supplementary Fig. S7e–g) or the extent of APAP-induced hepatocyte apoptosis (Supplementary Fig. S7h, i). These findings suggest that mtDNA fragmentation in APAP-treated cells occurs independently of FEN1-mediated processing.

Additionally, it has been suggested that short oxidized mtDNA fragments are transported into the cytoplasm via the mitochondrial permeability transition pore (mPTP)-VDAC1 transport axis[35]. In our study, pharmacological inhibition of mPTP using cyclosporine A (CsA) resulted in a partial reduction in cytoplasmic oxidized mtDNA levels (Fig. 4k, l; Supplementary Fig. S7j) and a corresponding attenuation of APAP-induced apoptosis (Fig. 4m, n). While previous reports indicate that mtDNA promotes VDAC1 oligomerization, thereby forming ion channels that facilitate mtDNA leakage from the mitochondrial intermembrane space to the cytoplasm[35], treatment with the VDAC1 oligomerization inhibitor VBIT-4 failed to reduce cytoplasmic oxidized mtDNA levels (Supplementary Fig. S7k, l) or mitigate APAP-induced apoptosis (Supplementary Fig. S7m, n).

These findings suggest that APAP-induced mtDNA fragmentation and cytoplasmic leakage occur through a distinct mechanism. We hypothesize that severe oxidative stress triggered by APAP leads to extensive mtDNA oxidation, promoting fragmentation in a nuclease-independent manner. Furthermore, the resulting oxidized mtDNA fragments may translocate into the cytoplasm via a pathway that is not fully dependent on the mPTP-VDAC1 transport system.

Oxidative modifications of DNA bases facilitate the B-to-Z DNA conformational transition

The administration of MitoQ for ROS clearance resulted in a reduction in Z-DNA levels, establishing a direct link between oxidative stress and the B-to-Z conformational transition of DNA[36]. In AML12 cells, APAP treatment induced a significant increase in PLA signal compared to controls, demonstrating robust proximity between Z-DNA and 8-oxoG (Fig. 5a, b). This result supports the notion that oxidative modifications drive the B-to-Z DNA transition.

To determine whether oxidative modifications alone are sufficient to induce the B-to-Z transition, we synthesized short dsDNA sequences (12 bp) containing six consecutive GC repeats, incorporating defined oxidation levels (0, 1, or 3 8-oxoG substitutions per strand) (Fig. 5c). The Z-DNA conformation was assessed using the A260/295 absorbance ratio as a readout, which is markedly reduced in Z-DNA relative to the canonical B-form[37]. The unmodified dsDNA initially displayed an A260/295 ratio of approximately 6, consistent with the B-form conformation (Fig. 5d). Upon substitution of guanine (G) with 8-oxoG, an inverse relationship emerged between the oxidation level and the A260/295 ratio, signifying a progressive transition from the B-form to the Z-conformation (Fig. 5d). Notably, while the canonical B-to-Z transition typically requires high-salt condition (≥ 2 M NaCl), this oxidation-driven structural shift occurred at low-salt concentration (20 mM NaCl), underscoring the unique ability of oxidative modifications to induce Z-DNA formation under physiologically relevant condition (Fig. 5d). The B-to-Z transition induced by oxidative modification was further validated through electrophoretic mobility shift assays (EMSA), which revealed specific binding of 8-oxoG-modified DNA to ZBP1 (Fig. 5e). Notably, this interaction was strictly dependent on the Zα domain of ZBP1, as evidenced by experiments using a mutated Zα domain that had lost its ability to bind Z-DNA (Fig. 5f). This domain-specific binding provides definitive evidence that the oxidized DNA adopts a left-handed Z-conformation, rather than merely representing a chemically modified B-form structure. Of note, the efficiency of Z-DNA formation was markedly enhanced in DNA strands containing three 8-oxoG substitutions compared to those with a single substitution

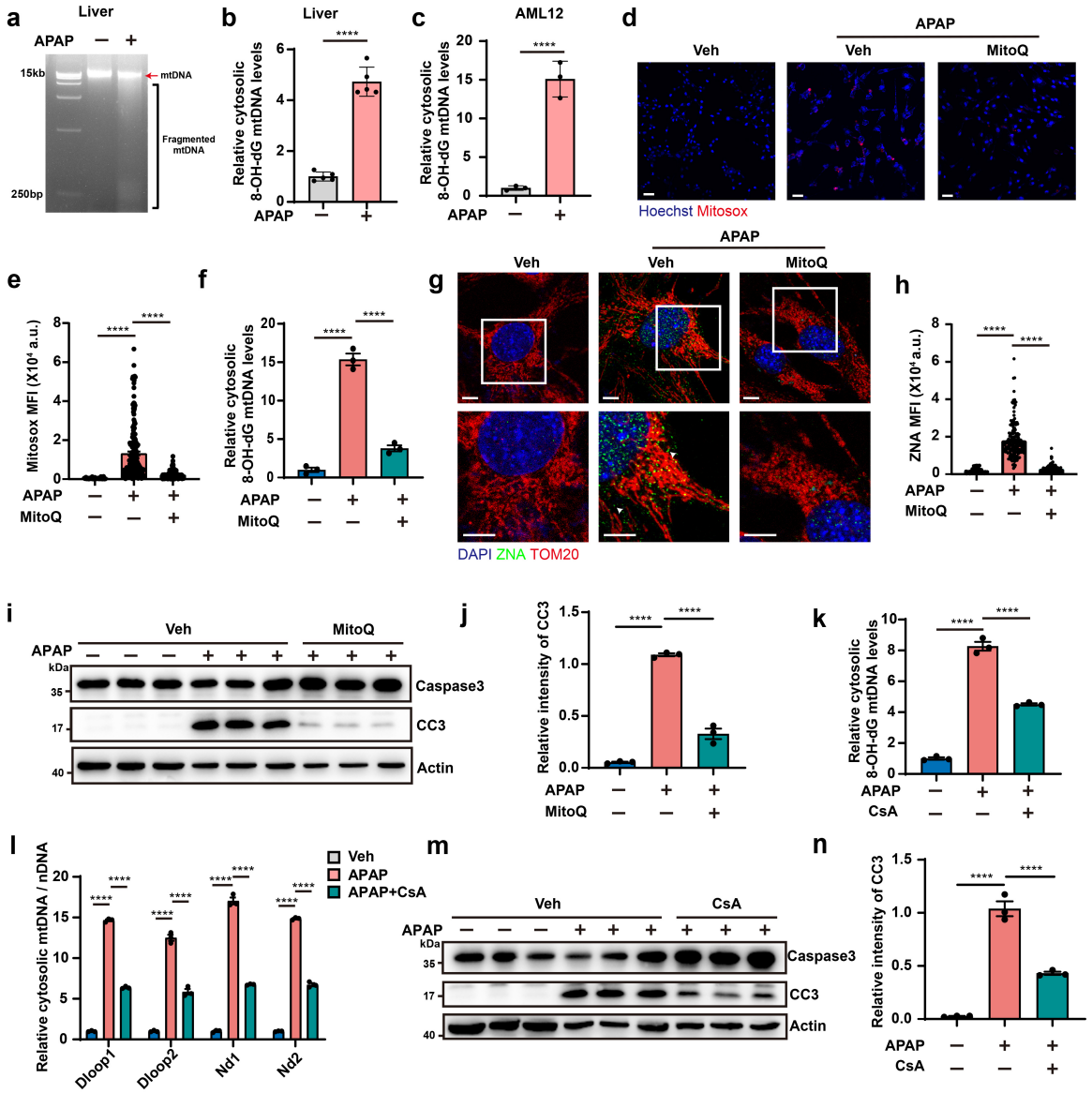

Fig. 4 Oxidative stress induces mtDNA fragmentation and cytoplasmic leakage in APAP-induced liver injury. a Agarose gel electrophoresis of mtDNA from liver of WT mice treated with or without APAP (300 mg/kg) for 24 h. **b** ELISA quantification of the amounts of cytosolic Ox-mtDNA in the liver of WT mice treated with or without APAP (300 mg/kg) for 24 h. *n* = 5 mice per group. **c** ELISA quantification of the amounts of cytosolic Ox-mtDNA in the AML12 cells treated with or without APAP (10 mM) for 24 h. *n* = 3 independent samples. **d** Representative images of mitoSOX Red^{+} cells indicating mitochondrial ROS production in AML12 cells treated with or without APAP (10 mM) for 24 h, in the presence or absence of MitoQ (1 μM). Scale bars, 50 μm. **e** Quantification analysis of the fluorescence intensity of MitoSOX Red per cell in **d**. *n* > 60 cells per group, repeated 3 times independently with similar results. **f** Quantification of the amounts of cytosolic Ox-mtDNA in the AML12 cells treated with or without APAP (10 mM) for 24 h, in the presence or absence of MitoQ (1 μM). *n* = 3 independent samples. **g** Immunofluorescence staining of ZNA (green) and TOM20 (red) in the AML12 cells treated with or without APAP (10 mM) for 24 h, in the presence or absence of MitoQ (1 μM). Scale bars, 10 μm. **h** Quantification of the percentage of ZNA-positive cells in **g**. n > 140 cells per group. **i**, **j** Western blotting (**i**) and quantification (**j**) analysis of the AML12 cells treated with or without APAP (10 mM) for 24 h, in the presence or absence of MitoQ (1 μM). *n* = 3 independent samples. **k** Quantification of the amounts of cytosolic Ox-mtDNA in AML12 cells treated with or without APAP (10 mM) for 24 h, in the presence or absence of CsA (10 μM). *n* = 3 independent samples. **l** Quantitative PCR analysis of cytosolic mtDNA release in cytosol fraction of AML12 cells treated with or without APAP (10 mM) for 24 h, in the presence or absence of CsA (10 μM). *n* = 3 independent samples. **m**, **n** Western blotting (**m**) and quantification (**n**) analysis of the AML12 cells treated with or without APAP (10 mM) for 24 h, in the presence or absence of CsA (10 μM). *n* = 3 independent samples. Data are mean ± SEM. Statistical analyses were performed using unpaired two-tailed Student's *t*-test (**b**, **c**) and one-way ANOVA post hoc Dunnett's tests (**e**, **f**, **h**, **j**–**l** and **n**); ns, not significant; $^{*}P < 0.05$; $^{**}P < 0.01$; $^{***}P < 0.001$; $^{****}P < 0.0001$. For gel source data, see Supplementary Data S1.

(Fig. 5e), further underscoring the critical role of cumulative oxidative modifications in driving the B-to-Z transition.

To further determine whether oxidative modification of DNA alone is sufficient to induce Z-DNA formation in cells, we transfected oxidized dsDNA into *Zbp1* KO mouse embryonic fibroblasts (MEFs). These cells lack both known Zα-binding proteins, ZBP1 and ADAR1-p150, with the latter exhibiting minimal expression in basal conditions[38]. In alignment with our biochemical data, the oxidized dsDNA adopted the Z-conformation intracellularly in the absence of ZBP1 and ADAR1-p150 (Fig. 5g–i). Thus, Z-DNA formation by oxidized dsDNA occurred independently of the stabilization by ZNA binding protein. Consistent with the *in vitro* results (Fig. 5e), Z-DNA formation in cells was significantly more efficient in DNA strands containing three 8-oxoG substitutions compared to those with a single substitution (Fig. 5g), further underscoring the ability of oxidative modifications to promote the B-to-Z transition in a cellular context. Notably, transfection of cells

with 8-oxoG-modified Z-DNA was sufficient to induce ZBP1-dependent cell death (Fig. 5j, k). Together, these findings robustly demonstrate that oxidative modifications alone are sufficient to drive the functional B-to-Z transition, both *in vitro* and in cells.

To investigate the reversibility of oxidative modifications in B-to-Z DNA transitions, we employed TH10785, a recently identified agonist of OGG1, to activate this DNA glycosylase that specifically removes oxidized guanine residues[4]. In *Zbp1* KO MEF cells transfected with oxidized dsDNA, OGG1 activation led to efficient removal of oxidative modifications, as evidenced by the loss of 8-oxoG signals (Fig. 5l, m). Concomitantly, DNAs were reverted from the Z-form to the B-form, as indicated by the disappearance of Z-DNA signals (Fig. 5l, n). These findings provide compelling evidence that oxidative modifications are sufficient to drive the B-to-Z DNA transition, and that this structural shift can be reversed through enzymatic deoxidation by OGG1.

Deoxidation facilitates Z-to-B DNA transition, protecting against APAP-induced liver failure and mortality

To assess the pathological relevance of oxidation-driven B-to-Z DNA transitions in APAP-induced liver injury, we examined hepatocyte cell lines following APAP treatment. APAP exposure promoted the formation of oxidized Z-DNA, while OGG1 agonist administration — whose mitochondrial accession we confirmed — efficiently reversed these oxidative modifications, restoring DNA to its B-form conformation (Fig. 6a–c; Supplementary Fig. S8a, b). This intervention significantly reduced cytoplasmic oxidized mtDNA levels and diminished Z-DNA content in both mitochondrial and cytoplasmic fractions (Fig. 6a). Notably, these molecular changes resulted in substantially attenuated cellular apoptosis (Supplementary Fig. S8c, d).

Consistently, in an APAP-induced liver injury model, treatment with the OGG1 agonist TH10785 substantially decreased cytoplasmic oxidized mtDNA levels (Fig. 6d; Supplementary Fig. S8e), which was accompanied by a corresponding reduction in Z-DNA (Fig. 6e, f). This molecular effect was associated with reduced apoptosis (as indicated by TUNEL staining and cleaved caspase-3) (Fig. 6g–j), diminished necrotic regions (Fig. 6k, l), decreased immune cell infiltration (Supplementary Fig. S8f–i), and overall preservation of liver function (Fig. 6m). Notably, the OGG1 agonist did not affect APAP metabolism in cells or the liver, as indicated by CYP2E1 (the key APAP-metabolizing enzyme) levels and GSH levels (Supplementary Fig. S9a–d). Additionally, it did not influence ROS production (Supplementary Fig. S9e, f) or ZBP1 expression levels (Supplementary Fig. S9g), confirming that its protective effects were specifically mediated through the direct removal of oxidative modifications from guanine in DNA. While TH10785 efficiently protected WT mice from APAP-induced hepatocyte apoptosis and liver injury, it completely failed to confer protection in *Ogg1* KO mice (Supplementary Fig. S9h–m) and *Ogg1*-knockdown cells (Supplementary Fig. S9n–p). This genetic evidence from both *in vivo* and *in vitro* models conclusively validates the on-target specificity of TH10785.

To evaluate the therapeutic potential of the OGG1 agonist in APAP-induced liver injury, we first examined its efficacy at a lethal APAP dose. Treatment with the OGG1 agonist conferred 90% protection against mortality (Supplementary Fig. S10a, b). To simulate a clinically relevant scenario, we employed a delayed-treatment model in which intervention was initiated 10 h post APAP administration (Fig. 6n). In this setting, the OGG1 agonist maintained a 90% survival rate, significantly surpassing the efficacy of N-acetylcysteine (NAC), the current clinical standard, which provided less than 50% protection (Fig. 6o). Strikingly, combining the OGG1 agonist with NAC resulted in 100% survival (Fig. 6o), demonstrating a synergistic therapeutic effect and underscoring the potential of this dual approach for clinical translation.

We note that TH10785 retained a milder, yet significant, protective effect in *Zbp1* KO and ZBP1-Zα mutant mice (Supplementary Fig. S10c), indicating that TH10785 also protects against ZBP1-independent cytotoxicity in APAP-induced liver injury.

DISCUSSION

In this study, we identify oxidative modification-driven B-to-Z transitions within mtDNA as the central pathological driver of APAP-induced ALF. Upon APAP exposure, oxidized mtDNA fragments leak into the cytosol, where they are recognized by the Zα domain of ZBP1, activating a downstream apoptotic signaling cascade (Supplementary Fig. S10d). During the preparation of this manuscript, another study demonstrated that amyloid-β (Aβ)-induced oxidative stress also promotes B-to-Z transition of mtDNA in microglia and contributes to neuroinflammation in Alzheimer's disease (AD)[39]. This finding, together with the current study, reinforces oxidative modification as a driving force for the B-to-Z conformational transition of DNA and implicates oxidized Z-DNA in the pathogenesis of various diseases. Our genetic data support a model in which ZBP1 engages MAVS to trigger caspase-8-dependent apoptosis, a pathway that operates independently of the canonical RIPK1 and FADD adaptors. This ZBP1-MAVS-caspase-8 axis is the principal cause of APAP-induced liver damage in our experimental model.

In addition to our finding that ZBP1 engages MAVS in the APAP context, we note that in other settings, ZBP1 signaling exhibits species- and context-dependent preferences — for instance, in murine cells, ZBP1 can induce necroptosis by directly complexing with RIPK3, whereas in human cells it may require RIPK1 to form a stable ZBP1–RIPK3 complex[20]. A key question arising from our work is how APAP stress directs ZBP1 toward this unconventional MAVS-dependent pathway. Our data showed that MAVS is not required for canonical ZBP1-dependent cell death induced by splicing inhibition (Supplementary Fig. S4q, r). Furthermore, using transfection of the Z-DNA oligonucleotide 8-oxodG$_3$dC, we observed that this Z-DNA ligand alone induces canonical ZBP1-RIPK3/RIPK1-dependent cell death in MEFs, independent of MAVS (data not sown). These observations indicate that the ZBP1-MAVS-caspase-8 axis is not dictated by the ligand (Z-DNA) alone, but rather by the unique redox microenvironment of hepatocytes during APAP overdose. We propose that APAP-induced mitochondrial ROS, or its electrophilic metabolite NAPQI — which forms protein adducts with cellular sulfhydryl groups — may alter the subcellular context. This could involve changes in MAVS oligomerization status, re-localization to mitochondria-associated membranes, or post-translational modifications of ZBP1, MAVS, or RIPK1, thereby biasing ZBP1 toward MAVS recruitment instead of RIPK1/FADD. Thus, the downstream signaling modality appears to be cell type- and context-dependent, not ligand-determined. The precise mechanisms governing ZBP1's choice of signaling partner —

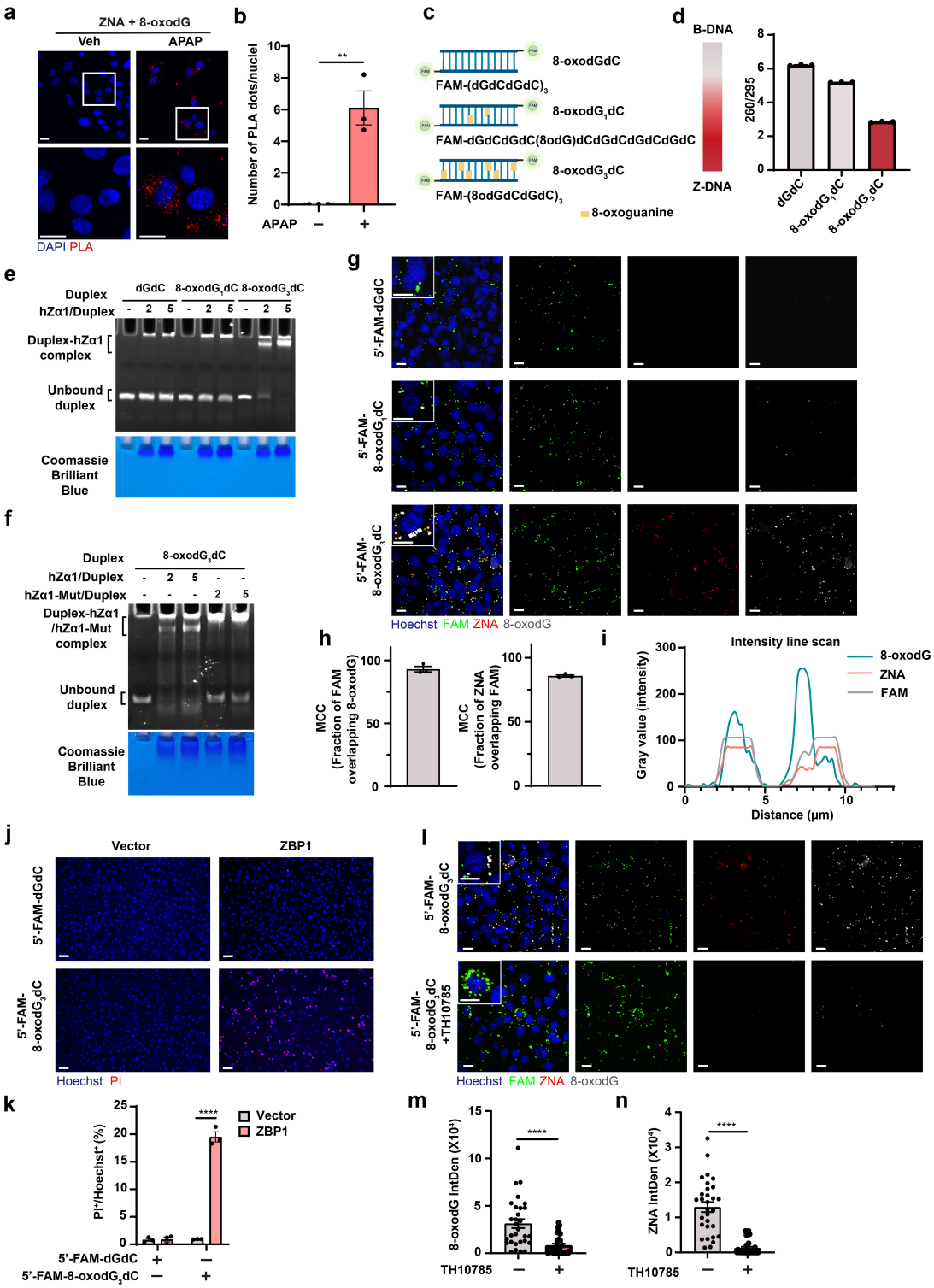

Fig. 5 Oxidative modifications of DNA bases facilitate the B-to-Z DNA conformational transition. a, **b** Representative image of PLA of ZNA-8-oxodG colocalization in AML12 treated with or without APAP (10 mM) for 24 h (**a**). Scale bars, 10 μm. Quantification is shown in **b**. *n* = 3 independent samples, *n* > 45 cells per sample. **c** Schematics of the synthesized dsDNA sequences (12 bp) containing six consecutive GC repeats with defined oxidation levels (0, 1, or 3 8-oxoG substitutions per strand). **d** Change of A260/295 as a measure of B-DNA (high ratio ~ 6) vs Z-DNA (lower ratio of ~3) formation is graphed. **e**, **f** EMSA assays of dGdC, 8-oxodG$_1$dC, and 8-oxodG$_3$dC duplexes incubated with hZα1 (the Zα1 domain of human ZBP1) at 1:2 and 1:5 duplex-to-protein molar ratios (**e**); and of 8-oxodG$_3$dC duplexes incubated with hZα1 and hZα1-Mut at 1:2 and 1:5 duplex-to-protein molar ratios (**f**). The concentration of each DNA duplex was 1 μM. **g** Immunofluorescence staining of FAM (green), ZNA (red) and 8-oxodG (gray) in the *Zbp1* KO MEFs transfected with dGdC, 8-oxodG$_1$dC and 8-oxodG$_3$dC duplexes, respectively. Dotted line indicates region chosen for intensity line scan analysis for **i**. Scale bars, 20 μm. **h** Quantification of percent of cells with FAM and 8-oxodG or ZNA overlap signal in **g**. *n* = 3 independent experiments. **i** Normalized intensity line scan of FAM, ZNA and 8oxodG in **g**. **j**, **k** Representative images (**j**) and quantitative analysis (**k**) of Hoechst and PI staining in *Zbp1* KO MEFs expressing either empty or ZBP1-WT, followed by transfection with 8-oxodG$_3$dC duplexes for 24 h. *n* = 3 independent samples. Scale bars, 200 μm. **l** Immunofluorescence staining of FAM (green), ZNA (red) and 8-oxodG (gray) in the *Zbp1* KO MEFs transfected with 8-oxodG$_3$dC duplexes for 24 h in the presence or absence of TH10785 (10 μM). Scale bars, 20 μm. **m, n** Quantification of the fluorescence intensity of 8-oxodG (**m**) and ZNA (**n**) in **l**. *n* = 10 cells per group, repeated 3 times independently with similar results. Data are mean ± SEM. Statistical analyses were performed using unpaired two-tailed Student's *t*-test (**b**, **k**, **m** and **n**). ns, not significant; **P* < 0.05; ***P* < 0.01; ****P* < 0.001; *****P* < 0.0001. For gel source data, see Supplementary Data S1.

RIPK1, RIPK3, or MAVS — remain an important subject for future investigation.

Our results further demonstrate that the OGG1 agonist TH10785 provides robust protection in WT mice, with efficacy superior to the standard clinical intervention NAC. Notably, it also retains a significant, though milder, protective effect in ZBP1-deficient models, indicating it mitigates both ZBP1-dependent and -independent cytotoxicity. As an agonist of OGG1, TH10785 promotes the repair of all oxidized DNA, including both mitochondrial and nuclear DNA. Our model proposes that APAP-induced mtDNA oxidation drives Z-DNA formation, its cytosolic release, and ZBP1-dependent cell death. However, the widespread oxidative stress induced by APAP also can cause nuclear DNA damage[40], which can trigger ZBP1-independent cytotoxicity through multiple well-established pathways, including PARP1 hyperactivation[41], ATM/ATR-mediated DNA damage responses[42], and transcriptional stress[43]. By globally reducing oxidative DNA damage, TH10785 simultaneously blocks both mtDNA-driven ZBP1-dependent death and nuclear DNA-driven ZBP1-independent death pathways. This dual action likely explains its superior efficacy compared to strategies targeting ZBP1 alone. Moreover, the liver possesses remarkable regenerative capacity. The initial response to excessive protein adduct formation after APAP overdose includes robust induction of autophagic pathways to clear damaged proteins and organelles[6]. An additional adaptive mechanism is mitochondrial biogenesis, which occurs selectively in surviving hepatocytes around areas of injury and is critical for liver recovery[6]. By preventing massive hepatocyte loss early after injury, TH10785 preserves tissue integrity and creates a permissive environment for these endogenous repair processes — including mitophagy and subsequent mitochondrial biogenesis — to operate effectively.

In summary, our findings establish the pivotal role of oxidation-driven B-to-Z DNA conformation transition in APAP hepatotoxicity. Our findings also highlight that promoting deoxidation via OGG1 activation facilitates the Z-to-B DNA transition, effectively mitigating hepatotoxicity and reducing mortality. This strategy represents a promising therapeutic avenue for improving clinical outcomes in APAP-induced ALF.

MATERIALS AND METHODS

Animal experiments

All animal experiments were approved by the Animal Care and Use Committee of Zhejiang University. *Zbp1*$^{-/-}$[21], *Ripk3*$^{-/-}$[44], *Mlkl*$^{-/-}$[45] mice were same as used[30]. *Zbp1*$^{Za1,2Mut/Za1,2Mut}$ mice were a gift from Dr. Jonathan Maelfait. *cGAS*$^{-/-}$ mice and *Mavs*$^{-/-}$ mice were initially from The Jackson Laboratory. *Ogg1*$^{-/-}$ mice were purchased from GemPharmatech (Strain No. T014260, GemPharmatech Co., Ltd.). *Ripk3*,*Casp8* DKO were generated by crossing *Ripk3*$^{-/-}$ mice with *Casp8*$^{-/-}$ mice[46]. *Casp8*$^{f/f}$ mice[47] were used as described. *Ripk1*,*Fadd*,*Ripk3* TKO mice were generated by crossing *Ripk3*$^{-/-}$ mice with *Ripk1*$^{+/-}$ mice[48] and *Fadd*$^{+/-}$ mice[49]. C57BL/6J mice (6- to 8-week-old) were purchased from Shanghai SLAC Laboratory Animal Co., Ltd. All mice were on a C57BL/6J genetic background and were bred, housed, and analyzed in the same specific facility at the Laboratory Animal Center of Zhejiang University. They were fed with a standard laboratory diet (Research Diets, D12450K, USA) and had free access to water in a constant temperature of 23 °C in a 12-h light/dark cycle. To induce liver injury with APAP, age-matched male mice were used; littermate WT controls were used in all experiments except those shown in Supplementary Fig. 4c. They were fasted for 16 h and injected intraperitoneally (i.p.) with either saline or APAP (Yuanye Bio-Tech Co., Shanghai, China) at 300, or 550 mg/kg body weight. The animals were anesthetized via isoflurane induction at various timepoints after APAP dosing for analyses. For all terminal (24 h) experiments, all injected mice were included in the analysis; no animals were excluded. To treat the animals with OGG1 agonist TH10785[4], the compound was dissolved in DMSO (Sigma-Aldrich) at a concentration of 100 μg/uL as a stock solution and diluted with 40% PEG300 and 5% Tween-80 to 0.5 mg/mL before use. TH10785 was injected i.p. at 5 μg/g. Following the planned treatment, the mice were anesthetized. Blood samples were obtained from the retroorbital venous plexus for analysis, and liver tissues were collected. Whole blood was centrifuged at 3,000× *g* and 4 °C for 10 min to separate the serum. Serum levels of ALT and AST were measured using commercial kits (Sigma-Aldrich, Shanghai, China). Liver tissues were fixed in 4% paraformaldehyde, dehydrated, and embedded in paraffin. Sections were cut at a thickness of 7 μm and collected for further examination. For histological analysis, tissue sections were stained with H&E. All histological assessments of tissue damage were performed by investigators blinded to the genotypes. Necrotic areas in H&E-stained sections were outlined and quantified using Adobe Photoshop under a 10× objective, and the percentage of necrotic area was calculated accordingly. For survival studies, mice were allowed to reach a natural endpoint, and the time post APAP injection was recorded.

Cell culture and stimulation

MEFs, AML12 and HepG2 cells were obtained in the lab. Cells were maintained in Dulbecco's modified Eagle's medium (DMEM) supplemented with 10% fetal bovine serum (FBS) and 1% (v/v) penicillin/streptomycin in an incubator supplied with a humidified atmosphere of 5% CO_2 at 37 °C. For primary hepatocytes, the mouse liver was perfused with 0.05% collagenase type IV (Sigma-Aldrich) to obtain primary hepatocytes, which were plated in round coverslips in DMEM with 10% FBS and 1% PenStrep for 4 h for attachment. Subsequently, the cells were used in immunofluorescence staining. AML12 cells and HepG2 cells were incubated with APAP (10 mM or 20 mM) for 24 h to establish an *in vitro* DILI model. APAP was dissolved into serum free DMEM directly. Cells were seeded in six-well plates before being subjected to treatments. Supernatants and cell lysates were collected for ELISA and immunoblot (IB) analyses. Protein sample of proliferating human hepatocytes (ProliHHs) was a gift from Dr. Lijian Hui[50].

Generation of KO and knockdown cell lines

The KO AML12 or HepG2 cell pools were generated using CRISPR/Cas9 methods. The target sequence for mouse *Ripk1* was: 5′-AGAAGAAGGGAACTATTCGC-3′. The target sequence for mouse *Fadd* was: 5′-TAGATCGTGTCGGCGCAGCG-3′. The target sequence for mouse *Zbp1* was: 5'-CAGGTGTTGAGCGATGACGG-3'. The target sequence for human *ZBP1* was: 5'-ATGTGAACCGAGACTTGTAC-3'. The target sequence for mouse *Mavs* was: 5′ -AGAGTCCCCAGAGTGTGTCC-3'. The target sequence for mouse *Casp8* was:5′ -GCAGGTCCCACCGACTGATG-3'. *Zbp1* knockdown by shRNA in AML12 cells was also used. Sequences of specific shRNAs used in this study were obtained from the MISSION shRNA Library (Sigma).

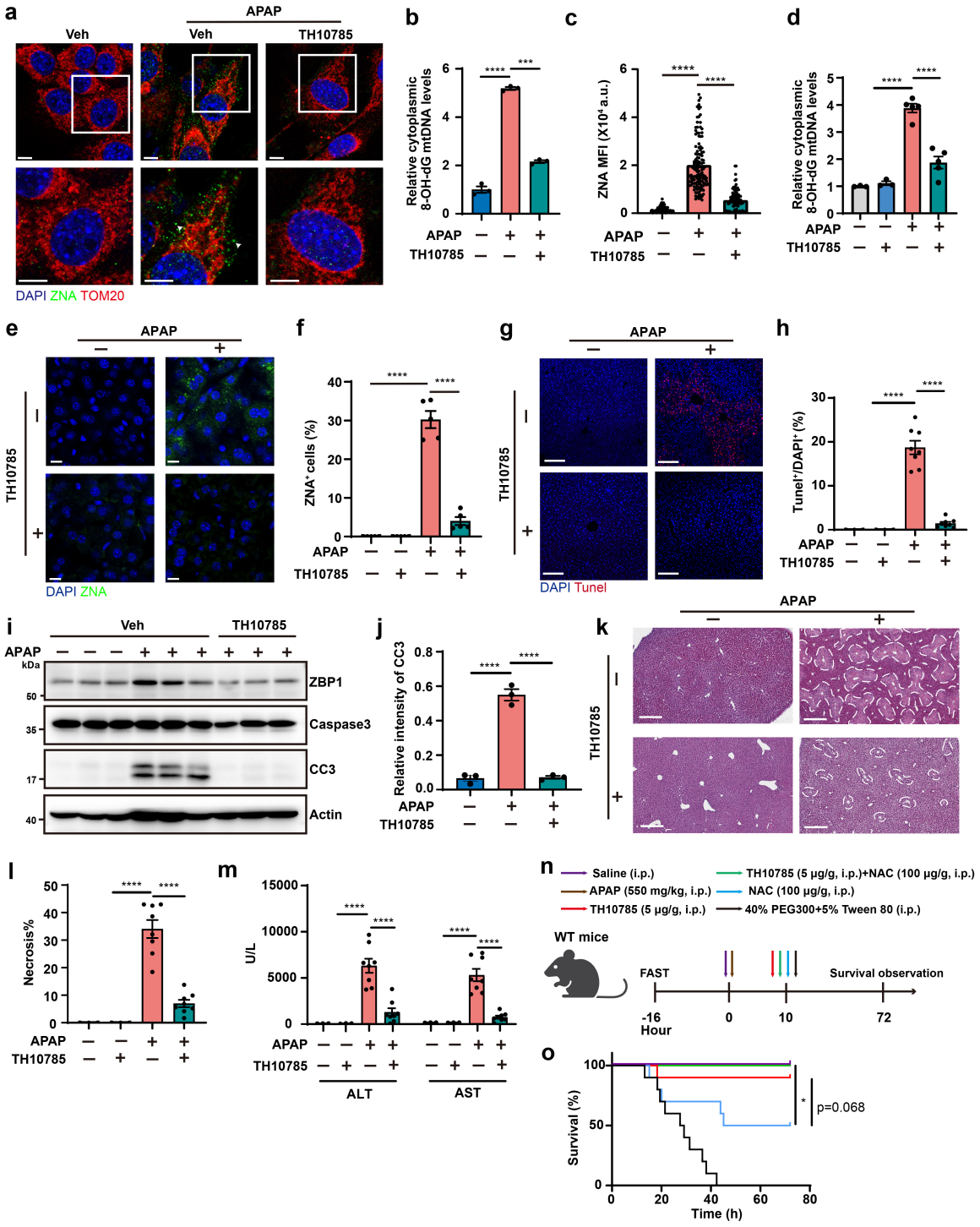

Fig. 6 Deoxidation facilitates Z-to-B DNA transition, protecting against APAP-induced liver failure and mortality. a Immunofluorescence staining of ZNA (green) and TOM20 (red) in AML12 cells treated with or without APAP (10 mM) for 24 h in the presence or absence of TH10785 (10 μM). Scale bars, 10 μm. **b** Quantification of the MFI (arbitrary units, a.u.) of the ZNA signals in **a**. $n > 90$ cells per group. **c** ELISA quantification of the amounts of cytosolic Ox-mtDNA in AML12 cells treated with or without APAP (10 mM) for 24 h, in the presence or absence of TH10785 (10 μM). $n = 3$ independent samples. **d** Quantification of the amounts of cytosolic Ox-mtDNA in the liver of WT mice treated with or without APAP (300 mg/kg) in the presence or absence of TH10785 (5 μg/g) for 24 h. **e**, **f** Immunofluorescence staining (**e**) and quantification (**f**) of Z-DNA-positive cells (green) in liver sections from WT mice treated with APAP (300 mg/kg) or vehicle control for 24 h, with or without co-administration of TH10785 (5 μg/g). Scale bars, 15 μm. **d**–**f** WT mice only treated with or without TH10785: $n = 3$ in **d** and $n = 5$ in **f**; WT mice treated with APAP in the presence or absence of TH10785: $n = 5$. **g**, **h** Representative images (**g**) and quantification analysis (**h**) of TUNEL staining in liver tissues from WT mice treated with or without APAP (300 mg/kg) in the presence or absence of TH10785 (5 μg/g) for 24 h. Scale bars, 100 μm. **i**, **j** Western blotting (**i**) and quantification (**j**) analyses of liver proteins from WT mice treated with or without APAP (300 mg/kg) in the presence or absence of TH10785 (5 μg/g) for 24 h. $n = 3$ mice per group. **k** H&E staining of the liver sections from WT mice treated with or without APAP (300 mg/kg) for 24 h in the presence or absence of TH10785 (5 μg/g). Scale bars, 300 μm. **l** Necrotic areas were encircled and quantified. **m** Serum ALT and AST levels were determined in WT mice treated with or without APAP (300 mg/kg) for 24 h in the presence or absence of TH10785 (5 μg/g). **g**, **h** and **k**–**m** WT mice only treated with or without TH10785: $n = 3$; WT mice treated with APAP in the presence or absence of TH10785: $n = 8$. **n** The scheme of APAP treatment in the presence or absence of TH10785 or NAC. **o** Survival curves of WT mice treated with a lethal dose of APAP (550 mg/kg i.p.) in the presence or absence of TH10785 or NAC, $n = 10$ mice per group. Data are mean ± SEM. Statistical analyses were performed using one-way ANOVA post hoc Dunnett's tests (**b**–**d**, **f**, **h**, **j**, **l** and **m**) and Mantel–Cox tests (**o**); ns, not significant; $^{*}P < 0.05$; $^{**}P < 0.01$; $^{***}P < 0.001$; $^{****}P < 0.0001$.

gRNA and shRNA were transduced into indicated cell line by lentiviral delivery. Cells were then subjected to blasticidin or puromycin selection.

siRNA transfection in AML12

For siRNA transfection in 24-well plates, a mixture containing 0.75 µL of siRNA duplexes (20 µM), 1.5 µL of Lipofectamin RNAiMAX reagent (Thermo Fisher Scientific, 13778150), and 75 µL of Opti-MEM (Gibco, 31985070) was incubated for 5 min and then added into AML12 culture for 24 h before treatment. The following oligonucleotide sequences were used for knockdown: si*Ogg1*,5'-AUAAGUGACAUCAUCAAGCUGTT-3'; si*Fen1*, 5'-CGUGCUAAUGCGACACUUATT-3'; siNC, 5'-UUCUCCGAACGUGUCACGUTT-3'; si*Mavs*, 5'-AGAUUCUAAAGGACGAAUACU-3'.

Lentivirus preparation and infection

HEK293T cells were transfected via calcium phosphate precipitation with lentiviral vectors encoding the cDNA or gRNA of interest, together with lentiviral packaging plasmids (pMD2.G and psPAX2). After 12 h, the culture medium was replaced. Viral supernatants were harvested 36 h post-transfection and used for subsequent infections. Target cells were incubated with lentivirus-containing supernatant supplemented with 10 µg/mL Polybrene and centrifuged at 2,500 rpm for 30 min to enhance transduction efficiency. The medium was refreshed 12 h after infection.

Cell death assay

For cell death assay by PI incorporation: briefly, 2×10^4 cells were seeded in 96-well plates. After 12 h, the cells were treated with reagents for the indicated durations. The cell death was also analyzed by the incorporation of PI. Briefly, the PI and Hoechst were added into medium when treatment. After treatment, three independent images per condition were captured by microscope, analyzed by Image J and the percent of PI-positive cells were averaged.

For cell apoptosis assay, an FITC Annexin V Apoptosis Detection Kit (Yeasen Biotech) was used. Briefly, cells were seeded in 12-well plates and cultured overnight. After indicated treatments, cells were harvested by mild trypsin digestion. The FITC-Annexin V and propidium iodide were used for double staining in accordance with the manufacturer's instructions, followed by analysis with Attune NxT flow cytometry (Thermo Fisher Scientific).

Caspase activity assay

Caspase-3 activity was measured using the Caspase-Glo® 3/7 Assay Kit (Promega, G8091), following the manufacturer's protocol. Briefly, 2.0×10^4 cells were seeded per well in white-walled 96-well plates (Nunc) and allowed to adhere for 12 h. Following experimental treatments, an equal volume of room temperature-equilibrated reagent was added directly to the culture medium. Plates were gently agitated for 5 min and then incubated at room temperature for 30 min. Luminescence was recorded using a microplate reader (Feyond-A300, ALLSHENG, China).

Subcellular fractionation of cells and tissues

In brief, cells were washed with ice-cold PBS while fresh tissues were minced into small pieces on ice. Both sample types were then homogenized using a glass Dounce homogenizer in Mitochondrial Preparation Buffer (0.225 M mannitol, 0.075 M sucrose, 20 mM HEPES, pH 7.4). The homogenates were centrifuged at 1,000× *g* for 10 min at 4 °C to pellet the nuclear fraction. The resulting post-nuclear supernatants were carefully transferred to new tubes and subjected to centrifugation at 12,000× *g* for 15 min at 4 °C, yielding cytosolic supernatants and pellets containing the mitochondrial fraction. The cytosolic fractions were reserved for subsequent analysis by ELISA or nucleic acid extraction. The mitochondrial pellets were either processed directly for DNA extraction using standard protocols or further purified for proteomic analysis by mass spectrometry.

Immunofluorescence staining

AML12 or MEF cells cultured in round coverslips were fixed in 4% PFA for 10 min and washed with PBS. After being permeabilized and blocked with 0.4% Triton X-100 and 3% BSA, cells were incubated with primary antibodies including 8oxodG (1:1,000, Abcam, ab48508), ZNA (1:1,000, Absolute Antibody, Ab00783-23.0), dsDNA (1:1,000, Abcam, ab27156), Tom20 (1:1,000, Proteintech, 11802-1-AP), TOM20 (1:1,000, Abclonal, A27799), PDHX (1:1,000, Proteintech, 10951-1-AP), ZNA (1:1,000, Absolute Antibody, Ab00783-3.0), ZNA (1:1,000, Novus Biologicals, NB100-749) antibody overnight at 4 °C. Then the cells were washed with PBS, incubated with secondary antibody for 1 h at RT. Images were captured by Olympus FV3000 or High Intelligent and Sensitive SIM (HIS-SIM).

Tissue immunofluorescence

The liver tissues were fixed in 4% paraformaldehyde, dehydrated in 15% and 30% sucrose, and embedded in optimal cutting temperature compound at −20 °C. The tissues were then sectioned (12 µm) using a cryostat. Afterwards, the sections were washed with PBS three times, blocked with 3% BSA and 0.4% Triton X-100 at RT for 1 h, and incubated with primary antibodies including CD45 (1:200, BD, 550539), Ly6G (1:200, Biolegend, 127601), cleaved Caspase-3 (1:1,000, CST, 9664S), Cleaved Caspase8 (1:1,000, CST, 8592) overnight at 4 °C. For ZNA staining in liver tissues, the tissues were pre-dried at 55 °C for 30 min and then subjected to proteinase K treatment (20 µg/mL) for 5 min at RT. When acquired, RNase A (1 mg/mL in PBS, Solarbio, 9001-99-4) or DNase I (25 U/mL in PBS, Invitrogen, AM2222) was used after proteinase K treatment at 37 °C for 1 h. The sections were incubated with primary antibody ZNA (1:1,000, Absolute Antibody, Ab00783-23.0) overnight at 4 °C, washed with PBS three times, and incubated with secondary antibody for 1 h at RT in the dark. Images were captured by Olympus FV3000 (fluorescence).

TUNEL staining

The principle of TDT-mediated dUTP nick-end labelling (TUNEL) to detect cell apoptosis is that the exposed 3′-OH of broken DNA can be catalysed by terminal deoxynucleotidyl transferase (TdT) with FITC-labelled dUTP, which can be detected using fluorescence microscopy. The specific steps were performed according to the kit's instructions (Vazyme, A113-03). Images were obtained by Olympus FV3000 (fluorescence). Digital images were recorded and analyzed using Image J software (NIH).

PLA

A PLA was employed to visualize protein–protein interactions, specifically assessing the associations between ZBP1 and

MAVS, as well as the proximity between ZNA and 8-oxodG. Briefly, AML12 cells grown on coverslips in 24‐well plates were treated as indicated. After fixation with 4% paraformaldehyde and permeabilization with 0.05% Triton X‐100 in PBS, cells were incubated overnight at 4 ℃ with species-matched primary antibody pairs against the targets of interest. The following antibodies were used (all at 1:100 for PLA): anti-ZBP1 (AdipoGen, AG-20B-0010-C100), anti-MAVS (HUABIO, HA721310), anti-ZNA (Absolute Antibody, Ab00783-23.0), anti-8oxodG (Abcam, ab48508).

Following primary antibody incubation, cells were probed with species-specific PLA secondary antibodies conjugated to oligonucleotides (rabbit MINUS, Sigma DUO92004, 1:5; mouse PLUS, Sigma DUO92002, 1:5). Subsequent ligation and amplification steps were performed according to the manufacturer's protocol (Sigma DUO92008). Samples were mounted using DAPI-Fluoromount-G (Beyotime, P0131) and imaged with Olympus FV3000 (fluorescence). Image processing and analysis were conducted using ImageJ software.

Intensity line measurement

Representative images for intensity measurement were captured by Olympus FV3000, and pixel intensity was assessed with Fiji (ImageJ) to measure indicated staining (ZNA/8oxodG/FAM) intensity across the dotted lines at baseline and after APAP-treated AML12 cells or FAM-8oxo-dG_3dC duplexes-transfected cells.

Automatic image analysis

For the quantification of mitochondrial superoxide, the intensity of the mitochondrial superoxide indicator MitoSOX was analyzed within cells using Hoechst as the nuclear counterstain and cells were defined by propagation of the nuclear objects to the cellular periphery on the basis of MitoSOX staining. For the quantification of cytoplasmic dsDNA and ZNA, the intensity of the cytoplasmic dsDNA and ZNA fluorescence intensity was analyzed within cells using DAPI as the nuclear counterstain and cells were defined by propagation of the nuclear objects to the cellular periphery on the basis of dsDNA staining. Statistical analysis of CD45 and Ly6G fluorescence was performed using ImageJ to calculate the percentage of area positive for each marker within the field of view. To quantify the colocalization of FAM/ZNA or FAM/8oxodG, the Manders' colocalization coefficient (MCC) was calculated using ImageJ software. First, dual-channel fluorescence images under a 60× objective were acquired under identical acquisition settings to ensure consistency. The images were then opened in ImageJ, and background subtraction was performed to minimize noise interference. The "Coloc JACop" plugin in ImageJ was utilized for the analysis.

Measurement of B-DNA and Z-DNA conformation using a ratio of A260/295

Conformation of Z-DNA and B-DNA was assessed using the absorbance ratio of 260 to 295 nm as previously described [51,52]. We used short dsDNA sequences (12 bp) with six consecutive GC repeats with defined oxidation levels (0, 1, or 3 8-oxodG substitutions per strand) (100 ng/μL) for conformation analysis. Poly(dG:dC) was diluted in annealing buffer (20 mM NaCl, 20mM Tris-HCL, 0.1mM EDTA) to induce Z-DNA conformation. A260/295 was measured with a NanoDrop (Thermo Fisher Scientific) using annealing buffer as a blank. Each incubation was performed in triplicates. The values were then plotted as the ratio of A260/295.

dsDNA transfection

For dsDNA transfection in 96-well plates, 0.1 μg of DNA duplexes were mixed with Lipofectamine 2000 (Thermo Fisher Scientific, 11668030) and brought up to 20 μL in Opti-MEM and allowed to sit at room temperature for 20 min. The mixture was then added to the MEF cells and allowed to incubate at 37 ℃ for 8 h. The medium was changed 8 h post transfection.

Generation of mtDNA-depleted AML12 cells

To establish mtDNA-depleted AML12 cells, the AML12 cell line was cultured for six days in medium supplemented with 400 ng/mL EtBr (Sangon, A500328) before proceeding with the indicated treatments. To evaluate the efficiency of mtDNA depletion, total DNA was extracted and subjected to real-time quantitative PCR. The expression levels of mitochondrial genes (*D-loop-1*, *D-loop-2*, *Nd1*, and *Nd2*) were measured, and the values from each replicate were normalized to the nuclear-encoded gene *Tert*.

EMSA

The binding assays were performed by incubating 2.5 μM of FAM-dGdC, FAM-8oxo-dG_1dC, and FAM-8oxo-dG_3dC oligonucleotides in 10 mM HEPES buffer (pH 7.5, containing 10 mM $MgCl_2$) with either reconstituted Human-ZBP1-Zα1 or its mutant form (Human-ZBP1-Zα1 with N46A and Y50A mutants) at specified DNA:protein molar ratios. The incubation was carried out for 2.5 h at 25 ℃. Following incubation, the DNA–protein complexes were separated by native polyacrylamide gel electrophoresis using 15% TBE gels. DNA visualization was achieved through post-staining withEtBr, and the resulting bands were captured using the Magic SHST's Gel doc system.

ELISA

For the measurement of cGAMP, AML12 cells were digested and collected into centrifuge tubes, and cells were counted using the Countstar automated after two washes with cold PBS. Cells were lysed by repeated freeze-thaw cycles in PBS at a ratio of 100 μL per million cells. Mice were euthanized, and the liver tissues were carefully dissected. A total of 1 mL of PBS was used for every 100 mg of fresh mouse liver tissue, which were then thoroughly disrupted using Tissuelyser-II (Shanghai Jingxin). Tissue homogenates were placed into a 3D shaker at 4 ℃ for 5 min before centrifuging. The Pierce BCA Protein Assay was used to normalize the protein concentration of the supernatants. The 2′ 3′ -cGAMP concentrations were measured using ELISA (COIBO, CB15107-Mu) according to the manufacturer's instructions. For the measurement of Ox-mtDNA, purified mtDNA was extracted from the cytosolic or mitochondrial fractions as indicated. The 8-OH-dG content was then quantified using 8-hydroxy 2-deoxyguanosine ELISA Kit (COIBO BIO, CB10013) according to manufacturer's instructions.

Immunoblotting

For mouse liver tissues, samples were collected from mice following cardiac perfusion with PBS, tissues were homogenized using metal beads at 60 Hz for 60 s in ice-cold RIPA lysis buffer (50 mM Tris-HCl, pH 7.5, 150 mM NaCl, 1% NP-40, 0.5% sodium deoxycholate, 0.1% SDS, 1% protease inhibitor cock-

tail, 1 mM PMSF, and 1% phosphatase inhibitor) with a TissueLyser II (QIAGEN), and centrifuged at 12,000× *g* at 4 ℃ for 30 min. Then the protein concentrations were adjusted to 1 mg/mL based on BCA. Proteins were blotted following a standard protocol. Antibodies against the following proteins were used for immunoblotting: ZBP1 (AdipoGen, AG-20B-0010-C100, 1:1,000), ZBP1 (Rabbit polyclonal antibody, generated in-house against the Zα domain of human ZBP1, 1:3,000), p-TBK1 S172 (CST, 5483S, 1:1,000), TBK1 (CST, 3013, 1:1,000), Cleaved Caspase-3 (CST, 9664S, 1:1,000), Caspase-3 (CST, 9662S, 1:1,000), p-MLKL (phospho S345)(Abcam, ab196436, 1:1,000), MLKL (Proteintech, 66675-1-Ig, 1:1,000), GSDME (Abcam, ab215191,1:1,000), GSDMD (Abcam, ab209845, 1:1,000), RIPK1 (CST, 3493, 1:1,000), MAVS (HUABIO, HA721310, 1:1,000), Cleaved Caspase8 (CST, 8592, 1:1,000), Caspase8 (CST, 4790, 1:1,000), Cleaved Caspase9 (CST, 9509, 1:1,000), Caspase9 (CST, 9508S, 1:1,000), CYP2E1 (HUABIO, R1511-7, 1:1,000), Tom20 (Proteintech, 11802-1-AP, 1: 2,000), Lamin B (Proteintech, 66095-1-Ig, 1:5,000), HA (HUABIO, HA721750, 1:3,000), FLAG (Sigma, f3165, 1:3,000), Actin (Proteintech, 66009-1-Ig, 1:5,000), GAPDH (HUABIO, ET1601-4, 1:5,000), Vinculin (HUABIO, ET1705-94, 1:5,000) and Tubulin (Millipore, 05-829, 1:10,000). The signals were detected by Immobilon ECL Ultra Western HRP Substrate (Millipore).

Co-IP

Cells were harvested and lysed in a non-denaturing lysis buffer (50 mM Tris-HCl, pH 7.4, 150 mM NaCl, 5% Glycerol, 1% Triton X-100) supplemented with complete protease and phosphatase inhibitor cocktails. At 4 ℃ with rotation for 30 min, then the cell lysates were clarified by centrifugation at 12,000 rpm for 15 min at 4℃. For each immunoprecipitation reaction, a total of 500 μg to 1 mg of clarified lysate was used. Anti-FLAG M2 Magnetic Beads were equilibrated by washing three times with lysis buffer. The pre-cleared lysate was then incubated with 10 μL of the bead slurry overnight at 4 ℃ with constant rotation. The following day, the bead-bound complexes were isolated by placing the tube on a magnetic rack. The supernatant was carefully aspirated, and the beads were washed stringently four times with 1 mL of ice-cold lysis buffer. Finally, the specifically bound proteins were eluted from the beads by boiling in 2× SDS sample buffer for 10 min. The eluted proteins were then resolved by SDS-PAGE and analyzed by immunoblotting with antibodies against FLAG and HA.

Cytosolic DNA immunoprecipitation

Liver tissue samples were lysed on ice for 10 minutes using 1 m L of digitonin lysis buffer (150 mM NaCl, 20 mM HEPES, pH 7.4, 25 μg/mL digitonin). The lysates were then centrifuged twice at 13,000× *g* for 5 min at 4 ℃ to separate the soluble supernatant from the pellet, which contains the heavy membrane fraction. For ZBP1 immunoprecipitation, antibodies against ZBP1 and control IgG were used. Following overnight incubation at 4 ℃ with rotation, the samples were washed extensively. Co-precipitated DNA was extracted using phenol‑chloroform and quantified by real-time quantitative PCR. Results are expressed as relative expression levels compared to untreated controls.

Quantitative real-time PCR

Total RNA was isolated from mice liver using TRIzol reagent (Life Technologies). RNA concentration was measured using the Nanodrop spectrophotometer (Thermo Fisher Scientific). cDNA was prepared using 1 μg of RNA with HiScript III room temperature SuperMix kit (Vazyme), and reverse transcribed into cDNA. qPCR was performed with ChamQ Universal SYBR qPCR Master Mix (Vazyme) by the CFX Connect Real-Time PCR Detection System (Bio-Rad). Data were analyzed according to the ΔΔ*CT* method. *Actin* (encoding β-actin) was used as the reference gene for accurate normalization of qPCR data. To measure the abundance of cytosolic mtDNA, 10 ng/μL of template DNA was used for qPCR analysis, and expression values of each replicate (*D-loop-1*, *D-loop-2*, *Nd1*, and *Nd2*) were normalized against nuclear-encoded *Tert*. The sequences of gene-specific primers used for PCR are shown below.

Zbp1-F:5’-TTGAGCACAGGAGACAATCTG-3’,
Zbp1-R:5’-TTCAGGCGGTAAAGGACTTG-3’;
Ifnb1-F: 5’-CAGCTCCAAGAAAGGACGAAC-3’,
Ifnb1-R: 5’-GGCAGTGTAACTCTTCTGCAT-3’;
Tnf-F: 5’-CCCTCACACTCAGATCATCTTCT-3’,
Tnf-R: 5’- GCTACGACGTGGGCTACAG-3’;
Il6-F: 5’-TAGTCCTTCCTACCCCAATTTCC-3’,
Il6-R: 5’-TTGGTCCTTAGCCACTCCTTC-3’;
Il1b-F: 5’-GCAACTGTTCCTGAACTCAACT-3’,
Il1b-R: 5’-ATCTTTTGGGGTCCGTCAACT-3’;
Usp18-F: 5’-TTGGGCTCCTGAGGAAACC-3’,
Usp18-R: 5’-CGATGTTGTGTAAACCAACCAGA-3’;
Isg15-F: 5’-CCCCCATCATCTTTTATAACCAAC-3’,
Isg15-R:5’-CACAGTGATCAAGCATTTGCG-3’;
Oasl1-F: 5’-TCCTTCGGTTGGTCAAACAC-3’,
Oasl1-R: 5’-CAGGCATAGACAGTGAGCAG-3’;
Irf7-F: 5’-TGTTTGGAGACTGGCTATTGG-3’,
Irf7-R:5’-ATCCCTACGACCGAAATGCT-3’;
Tert-F: 5’-CTAGCTCATGTGTCAAGACCCTCTT-3’,
Tert-R:5’-GCCAGCACGTTTCTCTCGTT-3’;
D-loop-1-F: 5’-AATCTACCATCCTCCGTGAAACC-3’,
D-loop-1-R: 5’-TCAGTTTAGCTACCCCCAAGTTTAA-3’;
D-loop-2-F: 5’-TCCTCCGTGAAACCAACAA-3’,
D-loop-2-R: 5’-AGCGAGAAGAGGGGCATT-3’;
Nd1-F: 5’- CTAGCAGAAACAAACCGGGC-3’,
Nd1-R: 5’-CCGGCTGCGTATTCTACGTT-3’;
Nd2-F: 5’- CCATCAACTCAATCTCACTTCTATG-3’,
Nd2-R: 5’-GAATCCTGTTAGTGGTGGAAGG-3’;
Fen1-F: 5’-TTCACGGCCTTGCCAAACTAA-3’,
Fen1-R: 5’-ACAGCAATCAGGAACTGGTAGA-3’;
LINE1-F: TAGGAAATTAGTTTGAATAGGTGAGAGGGT,
LINE1-R: TCCAGAAGCTGTCAGGTTCTCTGGC;
RNA18S-F: GTAACCCGTTGAACCCCATT,
RNA18S-R: CCATCCAATCGGTAGTAGCG;
Actin-F: 5’-GGCTGTATTCCCCTCCATCG-3’,
Actin-R: 5’-CCAGTTGGTAACAATGCCATGT-3’;
Ogg1-F: 5’-TGGTTTTAGCTTCTGGACAGTC-3’,
Ogg1-R: 5’-TGGTTTTAGCTTCTGGACAGTC-3’.

Measurement of mitoROS

MitoSOX™ Red dye (Invitrogen, USA) is a cell-permeable probe that selectively accumulates in mitochondria, where it is oxidized by superoxide to yield red fluorescence (λex = 396 nm; λem = 610 nm). AML12 cells were seeded in 35-mm dishes and treated with 10 mM APAP for 24 h. After treatment, the medium was removed and the cells were washed three times with PBS. Subsequently, 1 mL of 5 μM MitoSOX working solution was added, and cells were incubated at 37 ℃ for 30 min in the dark. Following incubation, cells were

washed three times with PBS and counterstained with 1 μg/mL Hoechst for 10 min. Fluorescence images were acquired using an Olympus FV3000 confocal microscope.

Measurement of GSH

For GSH quantification in liver tissue, samples were homogenized in extraction buffer at a 1:10 (w/v) ratio. The homogenate was centrifuged at 10,000× *g* and 4 ℃ for 10 min to collect the supernatant. Total protein concentration was determined using a BCA assay kit. Subsequently, GSH levels were measured according to the manufacturer's protocol with a commercial GSH detection kit (S0053, Beyotime Biotechnology).

For cellular GSH analysis, cells were plated in 6‑well plates and allowed to adhere overnight. Following the indicated treatments, cells were harvested and counted. An equal number of cells (2×10^6 per sample) were used for GSH measurement with the same commercial kit (S0053, Beyotime Biotechnology), following the provided instructions.

Mass spectrometry analysis

LC-MS/MS analysis was conducted using SCIEX QTRAP 6500+ system triple quadrupole mass spectrometer connected with Exion LC system. Chromatographic separation was achieved on an ACQUITY UPLC HSS T3 column (100 mm × 2.1 mm, 1.8 μm) at 40 ℃. The mobile phase consisted of 0.1% formic acid in water (A) and 0.1% formic acid acetonitrile (B) at a flow rate of 0.4 mL/min. The gradient of mobile phase B was 0% in 1 min, 0% to 1% in 1 min, 1% to 6% in 1 min, held at 6% for 0.5 min, then 6% to 50% in 1 min, 50% to 75% in 1 min, held at 75% for 1.5 min, then 75% to 0% in 0.5 min, and held at 0% for 3.5 min. The sample volume injected was 5 μL. Mass spectrometer was operated in electrospray ionization-positive mode using the following settings: nitrogen, with a purity of 99.9%, served as the desolvation gas at a manipulation temperature of 500 ℃. The curtain gas was set at 35 L/min, the ion source gas 1 pressure was maintained at 55 psi, and ion source gas 2 pressure was maintained at 50 psi. The capillary voltage was set to 5500V. Mass transitions monitored were m/z 284.2 -> 168.1 and m/z 284.2 -> 140.1 for 8-oxodeoxyguanosine, m/z 268.1 -> 152.3 and m/z 268.1 -> 135.1 for deoxyguanosine, m/z 268.4 -> 186.1 and m/z 268.4 -> 169.2 for TH10785.

Quantification and statistical analysis

In vitro data are presented as mean ± SEM from a representative experiment with the indicated number of independent replicates. For *in vivo* studies, results are shown as mean ± SEM, with the sample size (n) specified for each group. Detailed statistical information — including exact *n* values, post-hoc comparisons, and significance levels — is provided in the corresponding figures and legends. All statistical analyses were conducted in GraphPad Prism 8.0, applying two-tailed unpaired Student's *t*-tests, one-way ANOVA, or two-way ANOVA as appropriate and noted in the figure legends. Survival curves were compared using the Mantel–Cox log-rank test. *P* value below 0.05 was considered statistically significant.

DATA AVAILABILITY

All data are available in the main text or the supplementary materials.

ACKNOWLEDGEMENTS

We thank professor Lijian Hui (Chinese Academy of Sciences) for kindly providing us with proliferating human hepatocytes (ProliHHs). The study was supported by the National Natural Science Foundation of China (32225016, 82588302, 82530046 to W.M.; 92581110 to Z.-H.Y.; 82203426, 82472742 to L.S.), the National Key R&D Program of China (2024YFA1306400 and 2021YFA1101401 to W.M.), the Zhejiang Provincial Natural Science Foundation of China (LHZSD25C070001 to W.M.; LR25H160001 to M.C.), the "Pioneer" and "Leading Goose" R&D Program of Zhejiang (2025C02110 to W.M.), the Noncommunicable Chronic Diseases-National Science and Technology Major Project (2024ZD0524900 to Z.-H.Y.).

AUTHOR CONTRIBUTIONS

Z.-H.Y. co-conceived the study, designed, optimized and supervised the majority of experiments and analysis, performed oxidized DNA analysis *in vitro* and in cells, conducted cell death assays, drafted and revised the manuscript, and co-acquired funding. B.-X.Z. performed the majority of animal experiments, histological staining, and immunofluorescence, conducted all statistical analyses, co-analyzed data, prepared figures and contributed to manuscript drafting. H.-F.Y. maintained and expanded all mouse strains, performed a subset of mouse functional assays and tissue staining, co-performed western blot analysis of tissue samples, and conducted quantitative real-time PCR. R.G. performed the majority of cell line-related experiments, including stimulation, western blotting, subcellular fractionation, mtDNA extraction and co-performed tissue western blot analysis. L.S. and M.C. optimized mouse liver function assays, the APAP-induced injury model and co-acquired funding. Z.-Y.C. conducted EMSA experiments for oxidized DNA. Q.C. performed mitochondrial ROS detection, functional analysis, and flow cytometry. L.W. and J.H. generated gene-knockdown cell lines and rescue/overexpression cell lines. L.Z. constructed and prepared relevant plasmids. H.J. provided the *Mavs* KO mouse strain. P.X. performed functional validation of *cGAS* KO mice. Q.W. optimized dosing conditions for TH10785. J.Z. performed grayscale analysis of western blots and quantitative fluorescence analysis. J.P. and S.F. co-performed mass spectrometry analysis of 8-oxodG and TH10785. H.Z. provided the *Ripk1*$^{+/-}$ and *Fadd*$^{+/-}$ mouse strains. X.S. and M.C. assisted in project conceptualization, co-designed and co-conceived the study, and co-analyzed data. W.M. conceptualized the project, designed the study, analyzed data, reviewed and edited the manuscript, and acquired funding.

COMPETING INTERESTS

The authors declare no competing interests.

REFERENCES

1. Smilkstein, M.J., Knapp, G.L., Kulig, K.W. & Rumack, B.H. Efficacy of oral N-acetylcysteine in the treatment of acetaminophen overdose. *N. Engl. J. Med.* **319**, 1557–1562 (1988).
2. Yoon, E., Babar, A., Choudhary, M., Kutner, M. & Pyrsopoulos, N. Acetaminophen-induced hepatotoxicity: a comprehensive update. *J. Clin. Transl. Hepatol.* **4**, 131–142 (2016).
3. Fromme, J.C., Bruner, S.D., Yang, W., Karplus, M. & Verdine, G.L. Product-assisted catalysis in base-excision DNA repair. *Nat. Struct. Biol.* **10**, 204–211 (2003).
4. Michel, M. et al. Small-molecule activation of OGG1 increases oxidative DNA

damage repair by gaining a new function. *Science* **376**, 1471–1476 (2022).
5. Tran, T. & Lee, W.M. DILI: new insights into diagnosis and management. *Curr. Hepat. Rep.* **12**, 53–58 (2013).
6. Jaeschke, H. & Ramachandran, A. Acetaminophen hepatotoxicity: paradigm for understanding mechanisms of drug-induced liver injury. *Annu. Rev. Pathol.* **19**, 453–478 (2024).
7. Han, D. et al. Regulation of drug-induced liver injury by signal transduction pathways: critical role of mitochondria. *Trends Pharmacol. Sci.* **34**, 243–253 (2013).
8. Nelson, S.D. Molecular mechanisms of the hepatotoxicity caused by acetaminophen. *Semin. Liver Dis.* **10**, 267–278 (1990).
9. Kon, K., Kim, J.S., Jaeschke, H. & Lemasters, J.J. Mitochondrial permeability transition in acetaminophen-induced necrosis and apoptosis of cultured mouse hepatocytes. *Hepatology* **40**, 1170–1179 (2004).
10. Umbaugh, D.S., Nguyen, N.T., Jaeschke, H. & Ramachandran, A. Mitochondrial membrane potential drives early change in mitochondrial morphology after acetaminophen exposure. *Toxicol. Sci.* **180**, 186–195 (2021).
11. McGill, M.R. & Jaeschke, H. Metabolism and disposition of acetaminophen: recent advances in relation to hepatotoxicity and diagnosis. *Pharm. Res.* **30**, 2174–2187 (2013).
12. Newman, L.E. & Shadel, G.S. Mitochondrial DNA release in innate immune signaling. *Annu. Rev. Biochem.* **92**, 299–332 (2023).
13. Hopfner, K.P. & Hornung, V. Molecular mechanisms and cellular functions of cGAS-STING signalling. *Nat. Rev. Mol. Cell Biol.* **21**, 501–521 (2020).
14. Lauterbach-Rivière, L. et al. Hepatitis B virus DNA is a substrate for the cGAS/STING pathway but is not sensed in infected hepatocytes. *Viruses* **12**, 592 (2020).
15. Thomsen, M.K. et al. Lack of immunological DNA sensing in hepatocytes facilitates hepatitis B virus infection. *Hepatology* **64**, 746–759 (2016).
16. Choubey, D. Cytosolic DNA sensor IFI16 proteins: potential molecular integrators of interactions among the aging hallmarks. *Ageing Res. Rev.* **82**, 101765 (2022).
17. Lugrin, J. & Martinon, F. The AIM2 inflammasome: sensor of pathogens and cellular perturbations. *Immunol. Rev.* **281**, 99–114 (2018).
18. Zhang, Z.Q. et al. The helicase DDX41 senses intracellular DNA mediated by the adaptor STING in dendritic cells. *Nat. Immunol.* **12**, 959–965 (2011).
19. Ishii, K.J. et al. TANK-binding kinase-1 delineates innate and adaptive immune responses to DNA vaccines. *Nature* **451**, 725–729 (2008).
20. Amusan, O.T. et al. RIPK1 is required for ZBP1-driven necroptosis in human cells. *PLoS Biol.* **23**, e3002845 (2025).
21. Yang, D.W. et al. ZBP1 mediates interferon-induced necroptosis. *Cell. Mol. Immunol.* **17**, 356–368 (2020).
22. Maelfait, J. & Rehwinkel, J. The Z-nucleic acid sensor ZBP1 in health and disease. *J. Exp. Med.* **220**, e20221156 (2023).
23. Schneider, A.T., Gautheron, J., Tacke, F., Vucur, M. & Luedde, T. Receptor interacting protein kinase 1 (RIPK1) in hepatocytes does not mediate murine acetaminophen toxicity. *Hepatology* **64**, 306–308 (2016).
24. El Maadidi, S. et al. A novel mitochondrial MAVS/Caspase-8 platform links RNA virus-induced innate antiviral signaling to Bax/Bak-independent apoptosis. *J. Immunol.* **192**, 1171–1183 (2014).
25. Lei, Y. et al. MAVS-mediated apoptosis and its inhibition by viral proteins. *PLoS One* **4**, e5466 (2009).
26. Nassour, J. et al. Telomere-to-mitochondria signalling by ZBP1 mediates replicative crisis. *Nature* **614**, 767–773 (2023).
27. Yang, Z.H. et al. ZBP1 senses splicing aberration through Z-RNA to promote cell death. *Mol. Cell* **85**, 1775–1789.e5 (2025).
28. He, J.F. et al. ZBP1 senses spliceosome stress through Z-RNA: DNA hybrid recognition. *Mol. Cell* **85**, 1790–1805.e7 (2025).
29. Zhang, T. et al. Influenza virus Z-RNAs induce ZBP1-mediated necroptosis. *Cell* **180**, 1115–1129.e13 (2020).
30. Wang, R.C. et al. Gut stem cell necroptosis by genome instability triggers bowel inflammation. *Nature* **580**, 386–390 (2020).
31. Lei, Y.J. et al. Cooperative sensing of mitochondrial DNA by ZBP1 and cGAS promotes cardiotoxicity. *Cell* **186**, 3013–3032.e22 (2023).
32. Jiao, H.P. et al. Z-nucleic-acid sensing triggers ZBP1-dependent necroptosis and inflammation. *Nature* **580**, 391–395 (2020).
33. Devos, M. et al. Sensing of endogenous nucleic acids by ZBP1 induces keratinocyte necroptosis and skin inflammation. *J. Exp. Med.* **217**, e20191913 (2020).
34. Xian, H.X. et al. Oxidized DNA fragments exit mitochondria via mPTP- and VDAC-dependent channels to activate NLRP3 inflammasome and interferon signaling. *Immunity* **55**, 1370–1385.e8 (2022).
35. Kim, J. et al. VDAC oligomers form mitochondrial pores to release mtDNA fragments and promote lupus-like disease. *Science* **366**, 1531–1536 (2019).
36. Wang, J.Q., Wang, S.R., Zhong, C., Tian, T. & Zhou, X. Novel insights into a major DNA oxidative lesion: its effects on Z-DNA stabilization. *Org. Biomol. Chem.* **13**, 8996–8999 (2015).
37. Möller, A., Nordheim, A., Kozlowski, S.A., Patel, D.J. & Rich, A. Bromination stabilizes poly(dG-dC) in the Z-DNA form under low-salt conditions. *Biochemistry* **23**, 54–62 (1984).
38. Zhang, T. et al. ADAR1 masks the cancer immunotherapeutic promise of ZBP1-driven necroptosis. *Nature* **606**, 594–602 (2022).
39. Song, Z.W. et al. Innate immune sensing of Z-nucleic acids by ZBP1-RIPK1 axis drives neuroinflammation in Alzheimer's disease. *Immunity* **58**, 2574–2592.e9 (2025).
40. Cover, C. et al. Peroxynitrite-induced mitochondrial and endonuclease-mediated nuclear DNA damage in acetaminophen hepatotoxicity. *J. Pharmacol. Exp. Ther.* **315**, 879–887 (2005).
41. Kołacz, K. & Robaszkiewicz, A. PARP1 at the crossroad of cellular senescence and nucleolar processes. *Ageing Res. Rev.* **94**, 102206 (2024).
42. Blackford, A.N. & Jackson, S.P. ATM, ATR, and DNA-PK: the trinity at the heart of the DNA damage response. *Mol. Cell* **66**, 801–817 (2017).
43. Lans, H., Hoeijmakers, J.H.J., Vermeulen, W. & Marteijn, J.A. The DNA damage response to transcription stress. *Nat. Rev. Mol. Cell Biol.* **20**, 766–784 (2019).
44. Newton, K., Sun, X.Q. & Dixit, V.M. Kinase RIP3 is dispensable for normal NF-κBs, signaling by the B-cell and T-cell receptors, tumor necrosis factor receptor 1, and Toll-like receptors 2 and 4. *Mol. Cell. Biol.* **24**, 1464–1469 (2004).
45. Wu, J.F. et al. *Mlkl* knockout mice demonstrate the indispensable role of Mlkl in necroptosis. *Cell Res.* **23**, 994–1006 (2013).
46. Zhang, Y.Y. et al. A unique death pathway keeps RIPK1 D325A mutant mice in check at embryonic day 10.5. *PLoS Biol.* **19**, e3001304 (2021).
47. Beisner, D.R., Ch'en, I.L., Kolla, R.V., Hoffmann, A. & Hedrick, S.M. Cutting edge: innate immunity conferred by B cells is regulated by caspase-8. *J. Immunol.* **175**, 3469–3473 (2005).
48. Zhang, X.X. et al. Ubiquitination of RIPK1 suppresses programmed cell death by regulating RIPK1 kinase activation during embryogenesis. *Nat. Commun.* **10**, 4158 (2019).
49. Zhang, X.X. et al. MLKL and FADD are critical for suppressing progressive lymphoproliferative disease and activating the NLRP3 inflammasome. *Cell Rep.* **16**, 3247–3259 (2016).
50. Zhang, K. et al. *In vitro* expansion of primary human hepatocytes with efficient liver repopulation capacity. *Cell Stem Cell* **23**, 806–819.e4 (2018).
51. Chaires, J.B. Allosteric conversion of Z DNA to an intercalated right-handed conformation by daunomycin. *J. Biol. Chem.* **261**, 8899–8907 (1986).
52. Buzzo, J.R. et al. Z-form extracellular DNA is a structural component of the bacterial biofilm matrix. *Cell* **184**, 5740–5758.e17 (2021).

ADDITIONAL INFORMATION

Supplementary information The online version contains supplementary material available at https://doi.org/10.15302/vita.2026.04.0029.

Correspondence and requests for materials should be addressed to Wei Mo, Zhang-Hua Yang or Mingyu Chen.

Reprints and permission information is available at https://www.vita-journal.com/.

© The Author(s) 2026. Published by Higher Education Press. This is an Open Access article distributed under the terms of the CC BY license (https://creativecommons.org/licenses/by/4.0/).